Thomas Leitner, BSc

Thermophysical properties of liquid aluminium determined by means of electromagnetic levitation

MASTER'S THESIS

to achieve the university degree of

Diplom-Ingenieur

Master's degree programme: Technical Physics

submitted to

Graz University of Technology

Supervisor

Ao.Univ.-Prof. Dipl.-Ing. Dr.techn. Gernot Pottlacher

Institute of Experimental Physics

Graz, September 2016

AFFIDAVIT

I declare that I have authored this thesis independently, that I have not used other than the declared sources/resources, and that I have explicitly indicated all material which has been quoted either literally or by content from the sources used. The text document uploaded to TUGRAZonline is identical to the present master‘s thesis.

Date

Signature

Nomenclature

γ	Surface tension
ρ	Density
ε	Spectral emissivity
CM	Centre of mass
EML	Electromagnetic Levitation
fps	Frames per second
LD	Large Drop
MBP	Maximum Bubble Pressure
MovAvg	Moving average
mp	Melting point
SD	Sessile Drop
vol%	Volume percent
at.%	Atomic percent

Abstract

Subject of this thesis was the investigation of the thermophysical properties surface tension and density of liquid aluminium by means of electromagnetic levitation. Common measurement techniques are less suitable or face problems when liquid metals and alloys are investigated, due to the high reactivity of the liquid metals. Therefore, a non-contact, container-less measurement technique is to favour. These requirements are fulfilled by the electromagnetic levitation setup of the thermophysics and metalphysics group at Graz University of Technology which allows the non-contact, container-less measurement of surface tension and density of metals in the liquid phase for different temperatures. These data are very valuable for metalworking industry since simulations are an inherent part of development and production (e.g. casting technology) and rely on precise data of the temperature dependence of surface tension and density (amongst other material properties). The measurement results for the surface tension of liquid aluminium obtained within this thesis show good agreement with reference data from literature whereas density data show a slight offset to lower density values. This thesis includes an uncertainty analysis, where also the experimental challenges faced during the measurements are considered and possible reasons for this discrepancy are discussed. As a conclusion, various ideas for improvement and extension of the experimental setup and data evaluation process are given in the outlook, which possibly can solve the faced experimental challenges.

Kurzfassung

In dieser Arbeit wurden thermophysikalische Eigenschaften wie Oberflächenspannung und Dichte von flüssigem Aluminium mittels elektromagnetischer Levitation untersucht. Für die Untersuchung flüssiger Metalle und Legierungen sind die üblichen Messmethoden nur schlecht geeignet beziehungsweise stellen das Messverfahren vor spezielle Herausforderungen, die auf die hohe Reaktivität von flüssigen Metallen zurückzuführen sind. Daher ist eine kontaktlose, behältnisfreie Methode zu favorisieren. Der elektromagnetische Levitationsaufbau an der Technischen Universität Graz erlaubt die kontaktlose, behältnisfreie Messung der Oberflächenspannung und Dichte von flüssigen Metallen und Legierungen für unterschiedliche Temperaturen. Diese Daten sind für die metallverarbeitende Industrie sehr wichtig, da hier das Gebiet der numerischen Simulationen ein wichtiger Bestandteil der Entwicklung und der Produktionsprozesse ist (z.B. Gießprozesse). Diese Simulationen benötigen präzise Daten der Temperaturabhängigkeit von Materialeigenschaften wie Oberflächenspannung und Dichte. Im Fall der Oberflächenspannung von flüssigem Aluminium wurde eine gute Übereinstimmung der gemessenen Daten mit Vergleichswerten aus der Literatur festgestellt; für die Dichtemessungen zeigte sich eine leichte Verschiebung der Daten zu geringeren Dichtewerten. Die Arbeit beinhaltet ferner eine Unsicherheitsanalyse, welche die aufgetretenen experimentellen Unsicherheiten miteinbezieht und die möglichen Ursachen für die Abweichung der Messwerte zur Literatur diskutiert. Abschließend werden in einem kurzen Ausblick verschiedene Verbesserungsvorschläge hinsichtlich Messaufbau und Datenverarbeitung diskutiert, welche mögliche Lösungen für die aufgetretenen experimentellen Problemstellungen darstellen.

Contents

1 Motivation

The term "thermophysical properties" of liquid metals and alloys refers to the temperature dependence of the physical properties of the material, e.g. surface tension, density, viscosity, enthalpy, specific heat capacity, thermal conductivity and specific electrical resistivity. Precise data of these thermophysical properties is not only very valuable for the validation of theoretic models but also very essential for the metalworking industry and related fields, since these data are a key input for simulations of the manufacturing processes as well as stress test simulations [1].

Within the thermophysics and metalphysics group at Graz University of Technology (TU Graz), an extensive knowledge was built up how to access many of those thermophysical properties listed above experimentally with sophisticated measurement setups, such as the exploding wire technique, four point probe measurement, differential scanning calorimetry and differential thermal analysis. During a recent research project[1], an additional measurement setup, the electromagnetic levitation (EML) setup, was established to be able to determine the surface tension of liquid metals and alloys. Besides the determination of surface tension, the EML setup can be used to measure density of the specimen, which allows to generate additional data sets to check data obtained by the exploding wire technique and vice versa.

Pure metals (nickel and copper) were investigated at the end of the FWF[1] project in order to benchmark the experimental setup by comparing the obtained data with those from literature. Aluminium was chosen to be the next pure metal of interest since aluminium was expected to behave different due to its significant different properties (lower density, lower melting point, high electrical conductivity) compared to the pure metals investigated before and therefore to cause experimental challenges. In addition, literature data obtained with an electromagnetic levitation setup are quite rare and literature data in general vary significantly depending on the measurement method and experimental conditions. This circumstance appears surprising since aluminium is one of the worldwide most important materials and thus interesting to investigate [2].

[1] FWF Project P 23838-N20: "Levitation - Measurement of surface tension and density by means of levitation"

2 Introduction to electromagnetic levitation

The aim of this chapter is to give a short introduction to the electromagnetic levitation method so that the main part (experimental measurements and discussion) of this thesis is comprehensible. Thus, theoretical derivations are skipped and only the fundamental equations are presented. For further details, the according literature sources are referenced. The same is true for the description of the present experimental setup, as it is described in detail in the PhD thesis of Kirmanj Aziz and in the PhD thesis of Alexander Schmon [3, 4].

The method of electromagnetic levitation allows the contact-free, container-less measurement of surface tension and density of liquid metals and alloys by levitating the specimen in a radio-frequency electromagnetic field. It has to be noted that the term electromagnetic levitation itself refers just to the method how the contact-free, container-less condition is ensured since the determination of surface tension with this technique is based on an additional experimental technique: The Oscillating Drop (OD).

Whereas the determination of density via electromagnetic levitation is rather straightforward concerning the theoretical principles, the oscillating drop is a substantially more sophisticated approach. A detailed discussion of the theoretical principles of the oscillating drop technique would go beyond the scope of this thesis and as a consequence is just briefly summarized to the key aspects that are needed to understand the further chapters. But first, the fundamentals of how to electromagnetically levitate the specimen are discussed.

2.1 Specimen levitation

In an electromagnetic levitation setup, an inhomogeneous radio frequency electromagnetic field generated by an alternating current flowing through the so called “levitation coils” is established. The high frequency current is usually supplied by a high frequency generator that couples the power into an external oscillating circuit consisting of the levitation coils as inductance and capacitors.

A specimen positioned inside the levitation coils with a vertical axis will experience a lifting force that counteracts gravity as soon as the high frequency field is “powered

on". This lifting force is a result of the eddy currents induced into the specimen by the electromagnetic field, which themselves create an electromagnetic field opposing the external field according to Lenz's law, as illustrated in Figure 2.1.

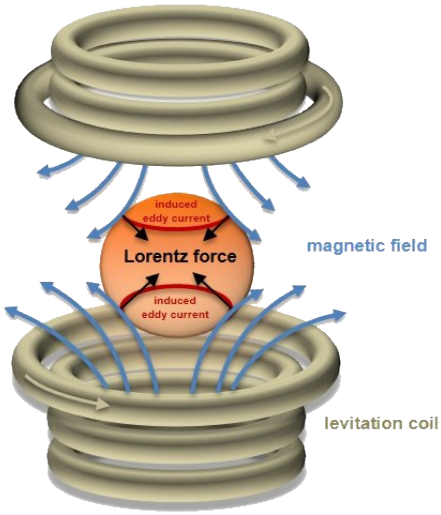

Figure 2.1: Illustration of the principle of electromagnetic levitation. Source of image: [4].

Thus, the specimen is pushed towards regions of lower field strength as the force F acting on the specimen is proportional to the gradient of magnetic induction B [5]

$$F(f(\sigma \cdot \omega), B) \propto -\nabla B^2 \tag{2.1}$$

with

f, g ... function
σ ... conductivity
ω ... angular velocity of the field.

In addition, the eddy currents heat the specimen due to the ohmic losses of the material. The heating power P absorbed by the specimen is proportional to [5]

$$P(g(\sigma \cdot \omega), \omega, B) \propto B^2 \cdot \omega. \tag{2.2}$$

As indicated by $F(f(\sigma \cdot \omega), B)$ and $P(g(\sigma \cdot \omega), \omega, B)$ in Eq. 2.1 and 2.2 respectively, levitation force and absorbed power both also depend on a function (f, g) of the product of conductivity of the sample material and angular velocity of the field $\sigma \cdot \omega$. It should be stated at this point that for an electromagnetic field with fixed parameters (field strength, frequency) a higher conductivity of the sample material usually yields in a

stronger levitation force. This is reasonable since the eddy currents generating the opposing field are larger due to the lower resistance. On the other hand absorbed power shows a maximum for a certain conductivity and decreases then for higher values of σ [6].

Another speciality of the electromagnetic levitation method is the phenomenon of stirring. Due to the eddy currents induced, turbulent specimen material flows occur in the levitated droplet. As a consequence, the specimen material is continuously mixed preventing segregation or similar effects. There are already numerical models that were validated with experimental results describing this phenomenon [7]. This phenomenon should be remembered for later discussion.

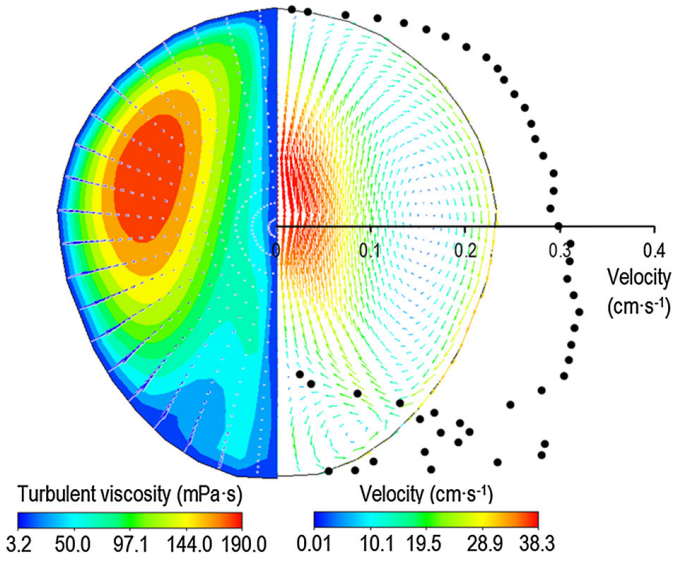

Figure 2.2: Simulation results of a numerical modelling approach to illustrate the phenomenon of stirring where turbulent flows across the specimen occur. Source of image: [7].

2.2 Oscillating Drop

As the specimen is levitated in the electromagnetic field, oscillations of the specimen's position can be observed. As soon as the specimen heats up to the melting temperature and passes the phase transition from solid to liquid, also oscillations around its equilibrium shape can be observed. These deformations from the equilibrium can be described mathematically by spherical harmonics where the change in radius of the specimen is described as the sum of spherical harmonics [6]

$$\delta R_0(\vartheta, \varphi, t) = \sum_{l \geq 0} \sum_{m=-l}^{m=+l} a_{l,m}(t) \cdot Y_l^m(\vartheta, \varphi) \tag{2.3}$$

with

$\delta R_0(\vartheta, \varphi, t)$ ... change in radius (deformation) as a function of polar angle θ, azimuthal angle φ and time t

$a_{l,m}(t)$ ... coefficient to the spherical harmonic Y_l^m (corresponds to the amplitude of deformation)

$Y_l^m(\vartheta, \varphi)$ ... real value of spherical harmonics.

The restoring force to the deformations is the surface tension of the liquid material. As a consequence, there must be a relation between the specimen's oscillations and the surface tension. Lord Rayleigh derived an equation that related the oscillations of non rotating, force-free spherical specimen to its surface tension [6]

$$\omega_l^2 = l \cdot (l-1) \cdot (l+2) \cdot \frac{4\pi}{3} \cdot \frac{\gamma}{M} \tag{2.4}$$

with

ω_l^2 ... angular velocity of oscillation

γ ... surface tension

M ... specimen's mass.

For $l < 2$, Eq. 2.4 yields zero. This is reasonable if one takes Eq. 2.3 into consideration since $l = 0$ describes just a change in radius which is forbidden due to the assumption of a droplet with constant density. The mode $l = 1$ describes a translation of the centre of mass as illustrated in Figure 2.3 which does not correspond to a surface oscillation of the droplet [8].

The first non-vanishing frequency (fundamental frequency) is obtained for $l = 2$ and is called "Rayleigh frequency", denoted as ω_R^2 [6]

$$\omega_R^2 = \frac{32\pi}{3} \frac{\gamma}{M}. \tag{2.5}$$

Under terrestrial conditions (e.g. in an electromagnetic levitation setup), gravity and Levitation-force (e.g. Lorentz-force due to the electromagnetic field) are acting on the specimen. Instead of a single oscillation frequency, three oscillation frequencies for $m = 0$, $|m| = 1$, $|m| = 2$ can be observed which are unequally spaced.

If the specimen is also rotating, the degeneracy of oscillation modes $m = |1|$ and $m = |2|$ splits up symmetrically [9] according to

$$\omega_{2,m}(\Omega) = \omega_{2,m}(0) + \frac{m}{l} \cdot \Omega \tag{2.6}$$

with Ω the rotational frequency and in total five oscillation frequencies for $m = -2$, $m = -1$, $m = 0$, $m = +1$, $m = +2$ may be observed, which are illustrated in Figure 2.4.

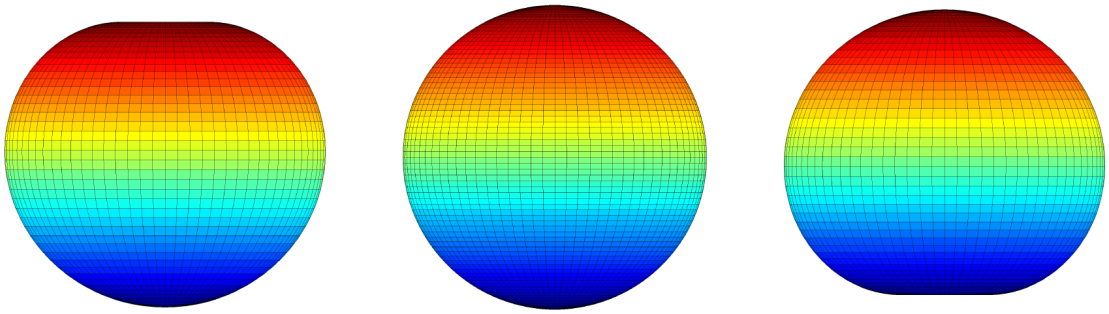

Figure 2.3: Illustration of the spherical harmonic for $l = 1$, $m = 0$ which corresponds to a asymmetric deformation and thus a translational motion of the centre of mass. Figure taken from [3].

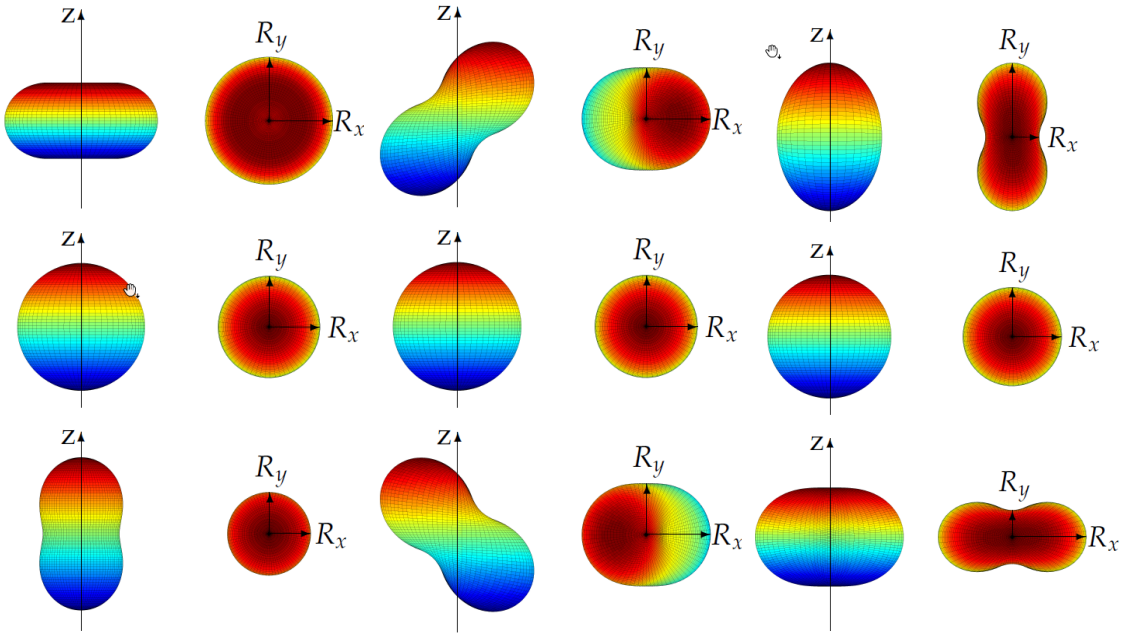

(a) $m = 0$ **(b)** $m = 1$ **(c)** $m = 2$

Figure 2.4: Illustration of the different oscillation modes for $l = 2$, $m = 0, 1, 2$, each from side and top view. Figure taken from [3].

Cummings and Blackburn [8] derived a correction for the Rayleigh frequency that yields the same results for the surface tension but is based on the shifted frequencies $\omega_{2,0}$, $\omega_{2,1}$, $\omega_{2,2}$. Since the split of $m = |1|$ and $m = |2|$ is symmetrical, $\omega_{2,1}$ and $\omega_{2,2}$ can be recovered [6] by

$$\omega_{2,m} = \frac{1}{2}\left(\omega_{2,m}(\Omega) + \omega_{2,-m}(\Omega)\right) \tag{2.7}$$

the correction of Cummings and Blackburn [8] can be applied

$$\omega_R^2 = \frac{1}{5} \cdot \left(\omega_{2,0}^2 + 2 \cdot \omega_{2,1}^2 + 2 \cdot \omega_{2,2}^2\right) - \overline{\omega_\tau^2} \cdot \left(1.90 + 1.20 \cdot \left(\frac{z_0}{a}\right)^2\right) \tag{2.8}$$

$$\overline{\omega_\tau^2} = \frac{1}{3} \cdot \sum_{i=1}^{3} \omega_i^2$$

$$z_0 = \frac{g}{2\overline{\omega_\tau^2}}$$

where z_0 corresponds to the relative position of the droplet in the field and with

g ... gravitational constant

ω_i ... translation frequency (x, y, z direction)

a ... radius of the specimen $(= \sqrt[3]{\frac{3 \cdot M}{4 \cdot \pi \cdot \rho}})$.

This approach obviously requires the distinct assignment of the oscillation frequencies to the oscillation modes. In case that this is not possible, the following equation is used where simply the sum over each squared oscillation frequency is calculated (adapted from [9])

$$\omega_R^2 = \frac{1}{5} \cdot \left(\sum_{m=-2}^{m=+2} \omega_{2,m}^2\right) - \overline{\omega_\tau^2} \cdot \left(1.90 + 1.20 \cdot \left(\frac{z_0}{a}\right)^2\right). \tag{2.9}$$

Both, Eq. 2.8 and 2.9 can be rewritten to frequencies instead of angular velocities and together with Eq. 2.5 the relations between surface tension, oscillation and translation frequencies can be expressed:

$$\gamma = \frac{3}{8} \cdot \pi \cdot M \cdot \left[\frac{1}{5} \cdot \left(\nu_{2,0}^2 + 2 \cdot \nu_{2,1}^2 + 2 \cdot \nu_{2,2}^2\right) - \nu_\tau^2 \cdot \left(1.9 + 1.2 \cdot \left(\frac{z_0}{a}\right)^2\right)\right] \tag{2.10}$$

$$\gamma = \frac{3}{8} \cdot \pi \cdot M \cdot \left[\frac{1}{5} \cdot \left(\sum_{m=-2}^{m=+2} \nu_{2,m}^2\right) - \nu_\tau^2 \cdot \left(1.9 + 1.2 \cdot \left(\frac{z_0}{a}\right)^2\right)\right] \tag{2.11}$$

with (a stays the same as in Eq. 2.8)

$$\nu_\tau^2 = \frac{1}{3} \cdot \sum_{i=1}^{3} \nu_i^2$$

$$z_0 = \frac{g}{2 \cdot (2 \cdot \pi \cdot \nu_\tau)^2}$$

Eq. 2.8 together with Eq. 2.7 is used if all five oscillation frequencies in the spectra can be assigned clearly to the individual oscillation modes, whereas Eq. 2.8 is used if this is not possible. The theoretical considerations on which these equations are based yield

moreover interesting relations between the oscillation modes that are important for the evaluation of the spectra and are thus briefly summarized at this point:

- According to Eq. 2.6, the frequency split due to the rotation of the drop is symmetrical and proportional to the oscillation mode index m. Thus, the split of the oscillation frequencies for $\nu_{2,\pm2}$ should be the double of the split of $\nu_{2,\pm1}$. This should be remembered for Section 3.5 since this aspect helps to assign the peaks in the spectrum to the different oscillation modes.
- If the vertical component of the electromagnetic field (parallel to gravity and the coils symmetry axis) varies linearly, Cummings and Blackburn showed [8] that the translational frequency in the direction of the field (ν_z) should be twice the value of the translational frequencies in the plane perpendicular to the field (ν_x, ν_y).

2.3 Experimental setup

The EML setup at TU Graz is illustrated in Figure 2.5. Key element is the probe chamber with three optical windows for monitoring the levitated specimen. The window at the top allows the acquisition of thermal radiation images of the specimen from a view in line with the vertical axis so that a rotational symmetry of the specimen on the images should be ensured. The other two windows are positioned on opposing sides in the horizontal plane and allow to acquire shadowgraph images by using a LED panel as background illumination. The pyrometer used for contact-less measurement of the temperature is positioned right aside the LED panel at a distance of approx. 250 mm from the expected levitation position of the specimen. Inside the probe chamber are the levitation coils made of watercooled copper tubes. The levitation coils are oppositely wound which "cages" the specimen between the two opposing electromagnetic fields from the bottom and top coil. At the bottom of the probe chamber is the sample holder (Al_2O_3) operated by a linear feedthrough from below the probe chamber.

Here a brief overview of the other components of the setup (details of the devices and their specifications are listed in the appendix on page 64):

Imaging system: The setup consists of two high speed cameras connected to a framegrabber card installed in the data processing computer and are used to observe the specimen from the top and side view. The thermal radiation images taken from the top view are used for determining the surface tension of the specimen whereas the shadowgraph images from the side view are used within density evaluation.

Evacuation system: The probe chamber can be evacuated via the installed vacuum system, consisting of a rotary vane pump and a turbomolecular pump in order to re-

move as much contaminants (e.g. oxygen) from the probe chamber as possible before flooding with an inert gas. Three different pressure gauges are installed for the different pressure ranges that are passed during the experimental procedure ($(10^{-6} - 10^{+3})$ mbar). A pressure regulating system is installed ensuring a constant pressure throughout the experiment in case of gas feed by controlling a valve to the rotary vane pump.

Gas supply: The atmosphere in the probe chamber is a crucial part during an electromagnetic levitation experiment since it ensures a clean environment and at the same time is responsible for the cooling of the specimen (see Section 3.2). The gas supply of the setup consists of four available high purity gases or gas mixtures (Alphagaz 1 Ar, Arcal 10, Alphagaz 2 He, custom mixture of He + 4 vol%H_2). It depends on the sample material characteristics which gas mixture is used during the experiment (more details in Section 3.2). In addition, a gas purification unit is installed to remove oxygen from the gas supply.

Power supply: The high frequency current is supplied by a high frequency generator operating at $f \approx 380$ kHz and delivers an alternating current of $I_{rms} \approx 350$ A to the external oscillator circuit consisting of the levitation coil as inductance and capacitors. All power supply components (high frequency generator, oscillator circuit) are cooled via a closed cooling-loop (with distilled water as coolant) by an external cooling unit to avoid the pipes to calcify. Only the levitation coil itself is directly cooled with tap water.

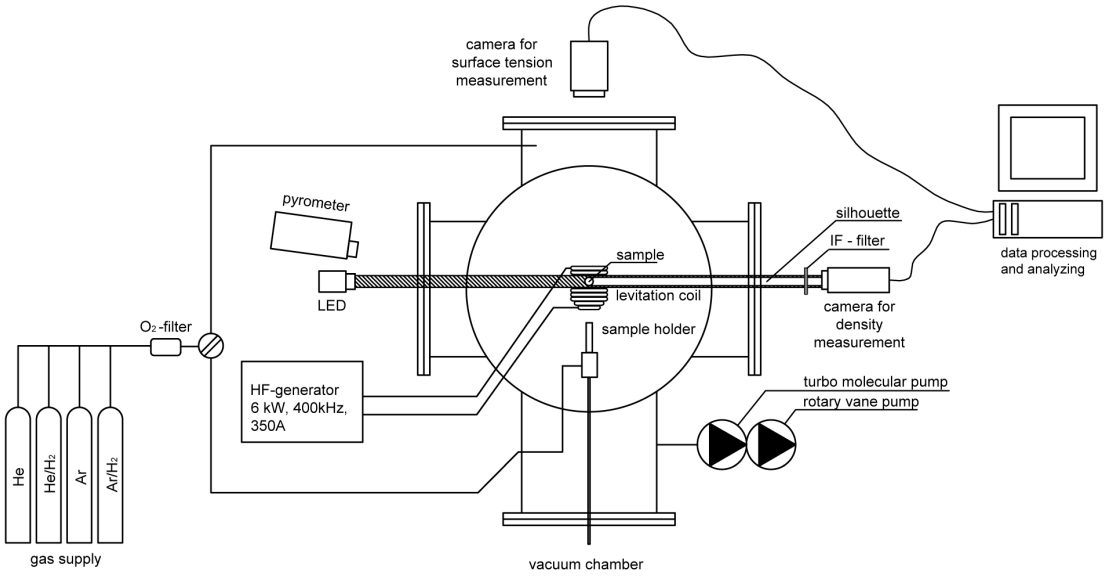

Figure 2.5: Depiction of the electromagnetic levitation setup at TU Graz. Figure adapted from [3, 4].

3 Measurement Procedure

3.1 Sample preparation

The aluminium samples investigated were cut off with a side cutter from a high purity (99.999 at.%)[1] aluminium rod with a diameter of 5.0 mm. Due to the (imprecise) usage of the side cutter, all samples slightly differed in weight but were within a range of approx. $(100 - 140)$ mg. This should not be seen as an imperfection since the sample weight adds an additional experimental quantity to test the measurement method against the (theoretical) independence from the sample weight. Each specimen was cleaned with acetone in an ultrasonic bath[2] for at least 10 minutes, followed by determining the specimen's weight with a precision balance[3].

3.2 Atmosphere

After weighing, the specimen was put on the specimen holder inside the probe chamber. The probe chamber was then evacuated to $< 5 \cdot 10^{-6}$ mbar in order to decrease the oxygen content in the atmosphere as much as possible. Immediately after the evacuation process, the probe chamber was flooded with Arcal 10[4], an inert gas mixture containing 97.6 vol% argon (Ar) and 2.4 vol% hydrogen (H_2), up to a pressure of 300 mbar to 800 mbar.

The gas atmosphere is a crucial part of the electromagnetic levitation experiment since it affects two fundamental processes: First, it is the key parameter to control the temperature of the specimen by heat dissipation from the specimen to the surrounding atmosphere. This is why a change in pressure and, more important, a change in composition of the gas atmosphere inside the probe chamber result in a change of specimen temperature. The heat dissipation from the specimen to the atmosphere thus can be increased/decreased by increasing/decreasing the pressure of the existing atmosphere or replacing the gas atmosphere with an inert gas with higher/lower heat convection,

[1] Advent Research, Batch No. Gi376; a certificate of analysis is attached on page 68
[2] Emag Technologies® Emmi®-20HC, for more details see the equipment list on page 64
[3] Mettler Toledo AB104-S-A, for more details see the equipment list on page 64
[4] Arcal 10: Ar + 2.4 vol% H_2; Impurities (ppm v/v): $H_2O \leq 40$, $O_2 \leq 20$, $N_2 \leq 80$

e.g. argon/helium (low/high heat convection). Second, the inert gas atmosphere hinders chemical reactions on the surface of the specimen, which is why inert gas mixtures of high purity must be used. For the investigation of aluminium, gas mixtures with small amounts of hydrogen (ARCAL 10 or He + 4 vol% H_2[5]) were chosen in order to possibly reduce aluminium oxide, covering the surface of the specimen, back to aluminium.

Due to the high electrical conductivity of aluminium, which lowers the heating for a given power induced, it was necessary to start the experiments with argon (providing a low heat convection) at a fairly low pressure of approx. 300 mbar in order to reach high specimen temperatures. Further lowering of the pressure (< 200 mbar) is in general not possible since sparks between the turns of the levitation coil would occur, resulting in an emergency shutdown of the high frequency generator. The maximum pressure is also limited, since the probe chamber is secured with a burst disc allowing only a little excess pressure (500 mbar) against ambient pressure in order to avoid the probe chamber's windows to break and its possible consequences, e.g. injuries of the experimenter. Thus a pressure of more than 1500 mbar must not be exceeded at any circumstance.

A stable temperature of the specimen is only obtained if the heat dissipation from the specimen (convection and thermal radiation) equals the heating from the ohmic losses of the induced eddy currents. Considering the fact that heating of the specimen is influenced by various parameters such as specimen size, levitation position, electromagnetic field of the coils, etc., it is evident that the needed variation in pressure or gas composition to achieve the desired specimen temperature is almost impossible to predict. The most practicable way to "control" the temperature of the specimen turned out to be a sequence of brief opening of the inlet valve and waiting for the system to balance. But even with those very small changes of the gas composition (e.g. adding helium), the desired temperature could be reached only within a range of 10 K. This is why the temperature scale was different for each measurement and not equidistant within an individual measurement.

3.3 Temperature measurement

The temperature of the specimen is measured contact-less by using a commercial pyrometer[6], operating in the bandwidth of $(1.45 - 1.80)\,\mu$m. The pyrometer measures the intensity of the incident infrared radiation and outputs the temperature of the specimens surface area targeted by the measurement spot. The inherent problem of single

[5] custom gas mixture: He + 4 vol% H_2; Impurities (ppm v/v) [3]: $N_2 \leq 40$, $O_2 \leq 5.0$, $H_20 \leq 5.0$, Hydrocarbon ≤ 1.0, Ne ≤ 10

[6] LUMASENSE TECHNOLOGIES, IMPAC IGA 6 ADVANCED, for more details see the equipment list on page 64

wavelength radiation thermometry is that emissivity ε of the object's surface is usually unknown and additionally may change with temperature.

Under the assumption that emissivity of the specimen surface does not change with temperature in the liquid phase, one can determine the real temperature by calibrating the pyrometer at a known reference temperature. As reference temperature the melting or solidification temperature of the specimen is used. Both temperatures can be extracted from the temperature versus time diagram where the melting/solidification plateau can be seen during the heat-up or cool-down process. Usually, the solidification plateau is less noisy due to the more homogeneous surface structure when going from the liquid to solid phase compared to the melting process and thus was the preferred reference point for the measurements.

During the measurement, the pyrometer is configured to use an emissivity of $\varepsilon = 1$, the temperature readings then correspond to the so called "*black temperature*" (T_B) of the specimen. A black body (thermal radiator) at this temperature would radiate the same intensity at this wavelength and thus give the same temperature reading on the pyrometer.

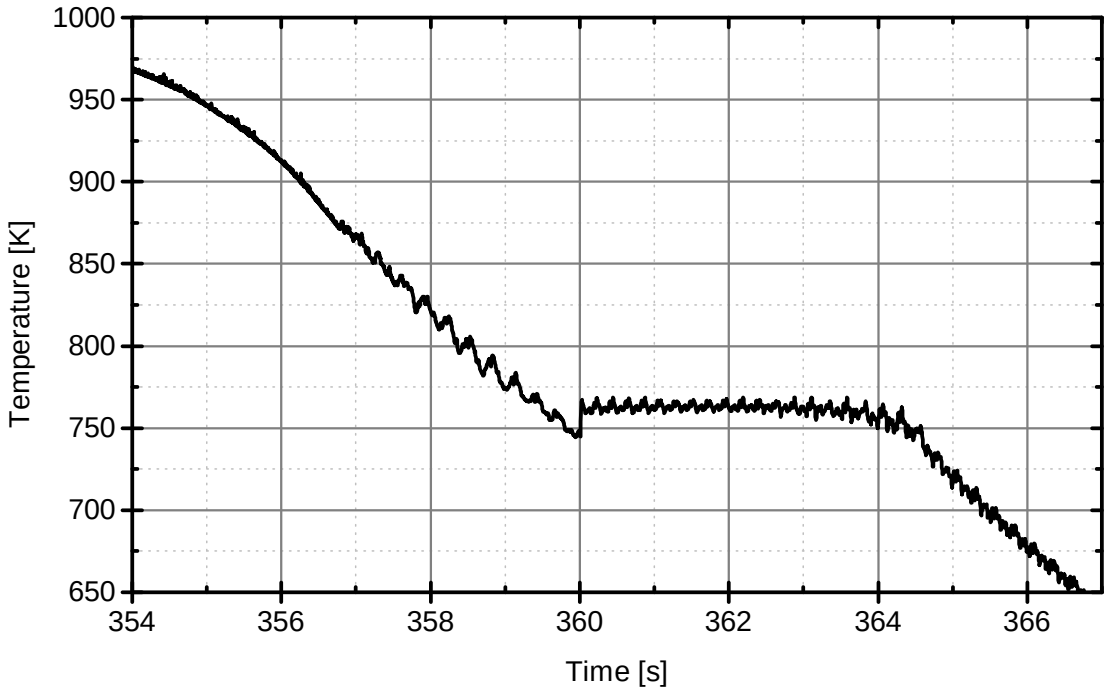

Figure 3.1: "Black temperature" (black line) of an aluminium specimen as a function of time during the cool-down process. The solidification plateau used to calibrate the pyrometer is clearly visible. Additionally, the specimen shows a slight undercooling before solidification.

By determining the black temperature of the solidification plateau (as illustrated in Figure 3.1), one can calculate the true emissivity at the solidification temperature [10]

$$\varepsilon = \exp\left(\frac{c \cdot h}{k \cdot \lambda}\left(\frac{1}{T} - \frac{1}{T_B}\right)\right) \tag{3.1}$$

with (source for constants and melting temperature: [11])

T ... real temperature at melting/solidification plateau (aluminium: 933 K)

T_B ... measured temperature at melting/solidification plateau

c ... speed of light in vacuum ($299\,792\,458\,\mathrm{m \cdot s^{-1}}$)

h ... Planck constant ($6.626068 \cdot 10^{-34}\,\mathrm{J \cdot s}$)

k ... Boltzmann constant ($1.380650 \cdot 10^{-23}\,\mathrm{J \cdot K^{-1}}$)

λ ... centre of pyrometer bandwidth ($1.625\,\mu$m).

Knowing the true emissivity at the solidification temperature and assuming that the emissivity does not change within the liquid phase ($\varepsilon = \text{const.} \neq f(T)$), one can recalculate the true temperatures from the black temperature readings [10]:

$$T = \left(\frac{1}{T_B} + \frac{k \cdot \lambda}{c \cdot h}\ln(\varepsilon)\right)^{-1} \tag{3.2}$$

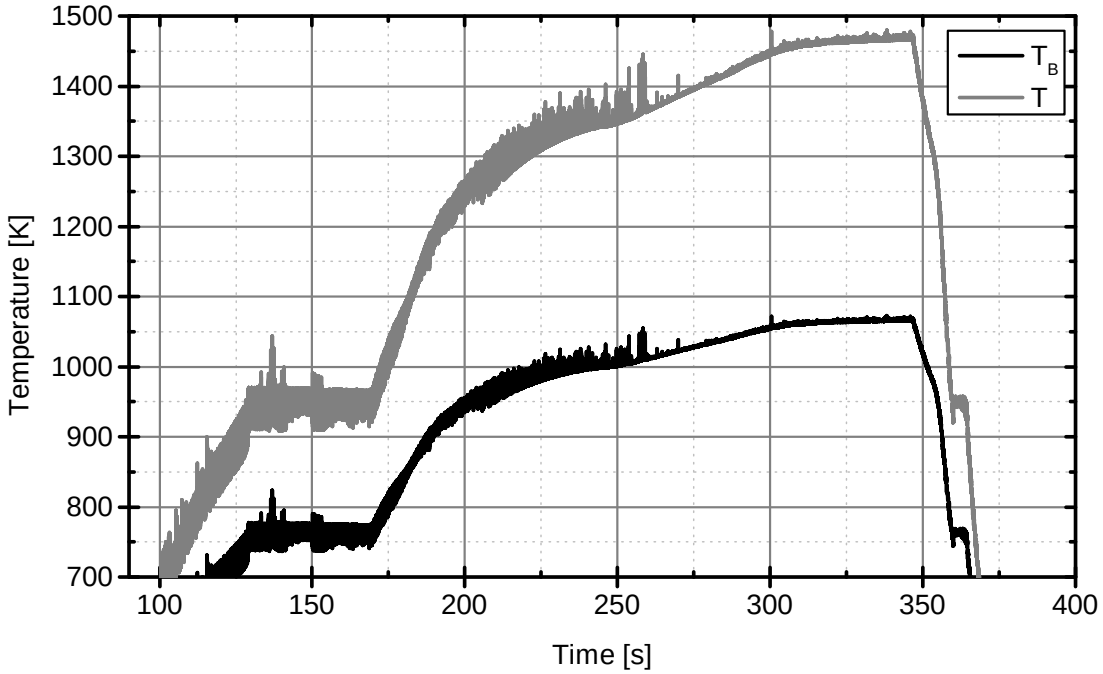

Figure 3.2: "Black temperature" (black line) and recalculated real temperature (red line) as a function of time for a complete melt and solidification run. Both, melting and solidification plateau can be observed, whereas the solidification plateau is clearly preferable for the calibration compared to the melting plateau due to the lower noise. Additionally, the signal appears to get more stable when reaching high temperatures. This will be discussed in Section 4.1 in more detail.

3.4 Execution of measurement

The specimen is positioned between the bottom and top part of the levitation coils using the sample holder on the linear feedthrough. By switching on the high frequency generator and ramp up the power to maximum, the high frequency field is established and the specimen starts to levitate. The sample holder is then pulled out from the levitation coil. The levitated specimen heats up to the melting point, performs the phase change to liquid and continues to heat up until an equilibrium between heat dissipation and heating power is reached. In the liquid phase, the specimen starts to perform oscillations (see Section 2.2).

During a measurement, the pressure and gas composition was varied to adjust the specimen's temperature to different stable values (see Section 3.2). For each temperature value, a series of max. 4100 images[7] of the specimen was taken, where the observation spot depended on the purpose of the measurement: For the determination of the sur-

[7] upper limit given by the amount of memory installed on the PC for data acquisition

face tension, direct images of the specimen were recorded from the top with camera 1 adjusted to frame rates greater than 200 fps (frames per second). In case of the density measurement, shadowgraphs from the side were recorded with camera 2 at 120 fps[8], using a green LED panel for background illumination and an interference filter in front of the object lens blocking infrared radiation from the specimen in order to increase the sharpness of the edges.

At the end of a measurement, the specimen is cooled below the melting point by directly blowing an inert gas mixture on the specimen through the specimen holder (aluminium oxide tube, see Section 2.3). When the specimen is solidified, the sample holder is positioned below the levitated specimen and is used to catch the specimen while the output power of the high frequency generator is reduced and switched off.

Each specimen was weighed after the measurement to detect evaporation of the sample material. The highest mass loss of all specimen was about 0.2 mg so it can be stated that evaporation is negligible during these experiments.

Reference images for density evaluation

In order to get an absolute (metric) value for the projected area of the specimen in the shadowgraphs, reference images of ball bearing spheres with known but different diameter were taken. By determining the size of the shadow area of those reference spheres, one can determine conversion factors for the area of the shadows between px^2 and m^2. The conversion factors for the different sized spheres were fitted with a linear fit in order to improve the precision. Now, a conversion factor can be calculated from this linear fit and the real (metric) shadow area of the specimen is obtained.

Levitating the reference spheres in the electromagnetic field would result in heating and melting, thus they were simply hovered for a short period at the approximate levitation position of the specimen by a gas flow from the bottom through the sample holder. During this short period, the shadowgraphs were recorded and afterwards sorted for the images where the reference sphere was freely visible and not in contact with the sample holder.

3.5 Data Evaluation

Evaluation of the recorded images was done by using a VISUAL C# program written by Kirmanj Aziz and Alexander Schmon and extended for additional output by myself. The program loads all images recorded at a single temperature point and evaluates position

[8] corresponds to the maximum frame rate of the used camera device (for details, see equipment list in appendix on page 64)

and size of the specimen in each image. Depending on the type of image recorded, either direct image for surface tension evaluation or shadowgraph image for density evaluation, the algorithm to determine the size of the specimen on the image is different.

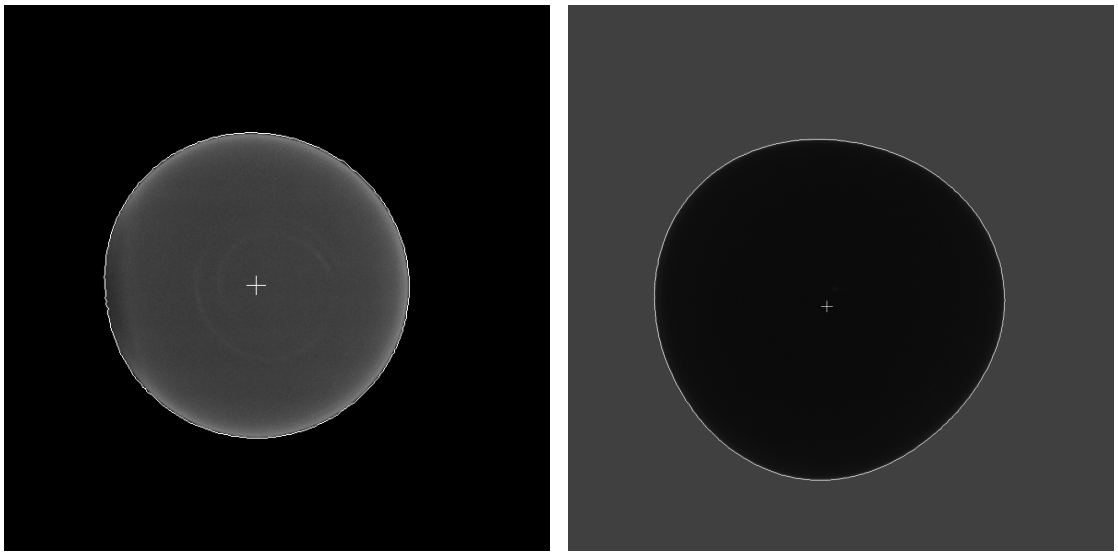

(a) Edge detection in case of surface tension evaluation (direct images of the specimen).

(b) Edge detection for shadowgraph images in case of density evaluation.

Figure 3.3: Screenshots of the software that performs the edge detection for each recorded image. In case of the surface tension evaluation, (direct) images of the thermal radiation of the specimen are processed (a). For the density evaluation, shadowgraph images of the specimen are analysed (b).

In the case of direct images for surface tension evaluation, the position and size of the specimen on the image is simply determined by detecting all pixels above an adjustable intensity threshold. Starting from the detected centre of mass (CM), the radius of the specimen area is determined in 5° steps.

For the density evaluation, a different algorithm is applied to detect the edge of the specimen, since the exact size of the shadow is crucial for precise results. Only the centre of mass is determined by the method applied for the surface tension images, whereas the position of the edge is determined by searching for the point of inflection in the polynomial fitted intensity profile along each radius (so called sub-pixel edge detection).

A further explanation of the mentioned algorithms would go beyond the scope of this thesis. For a more detailed description please take a look into the PhD thesis of Kirmanj Aziz [3] and PhD thesis of Alexander Schmon [4] respectively.

The software generates an ASCII - file, containing the coordinates of the centre of mass, the number of pixels of the specimen (corresponds to area in px^2) and all radii for each image of the image sequence.

Table 3.1: Comparison of the structure of the ASCII files generated by the edge detection software (filled with some sample data). Due to the high requirements in case of the density evaluation, the radii of the shadowgraph are determined in 1° steps, whereas for the surface tension evaluation, 5° steps provide a good trade-off between accuracy and computation time.

CM_x, CM_y	...	x and y coordinates of the centre of mass
N_{pix}	...	Number of pixels
r_φ	...	radius measured from the centre of mass to the detected edge in direction of angle φ

	CM_x[px]	CM_y[px]	N_{pix}[-]	$r_{0°}$[px]	$r_{5°}$[px]	...	$r_{355°}$[px]
1	276.788	306.038	86223.000	166.000	166.634	...	166.634
⋮	⋮	⋮	⋮	⋮	⋮	⋮	⋮
4099	276.247	305.887	86192.000	165.000	164.626	...	164.626

(a) Structure of the output file in case of surface tension evaluation (5° steps).

	CM_x[px]	CM_y[px]	N_{pix}[-]	$r_{0°}$[px]	$r_{1°}$[px]	...	$r_{359°}$[px]
1	487.008	525.694	301338.000	313.312	313.186	...	313.209
⋮	⋮	⋮	⋮	⋮	⋮	⋮	⋮
4099	490.783	542.579	305141.000	326.393	326.672	...	326.625

(b) Structure of the output file used for the further density evaluation (1° steps).

All the relevant information about the specimen (position, size, movement and oscillation) for the recorded time frame is now stored in the generated ASCII files. This usually very time-consuming image evaluation process has to be done only once and all further evaluation is based on this data.

Surface tension evaluation

The data of the generated ASCII files were processed with a MATLAB script, where a Fourier transform of all parameters in the ASCII files was performed to generate the according spectra. The peaks in the Fourier transform of the parameters CM_x and CM_y represent the translation frequencies (ν_x, ν_y) of the specimen in the horizontal plane (see Figure 3.4). The translation frequency in the vertical direction (ν_z) is assumed to be twice the value of the translation frequencies in the horizontal plane (ν_x, ν_y), according to theory (see Section 2.2). The correctness of this assumption was checked exemplarily by analysing a spectrum of the centre of mass of a single shadowgraph image sequence acquired with the density camera.

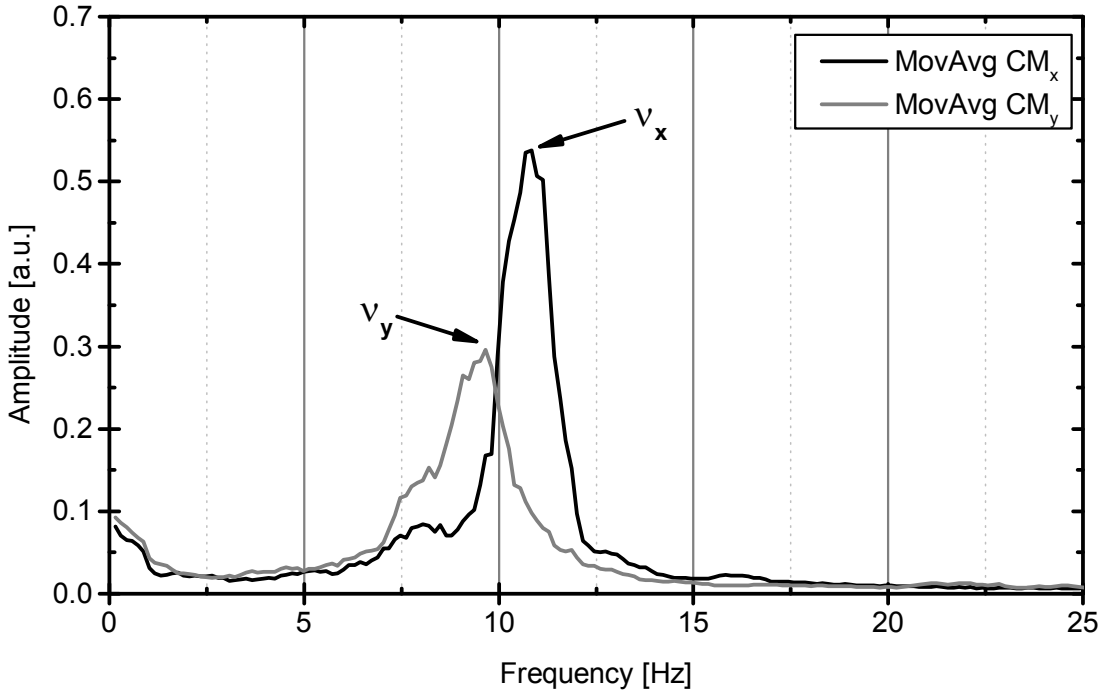

Figure 3.4: Spectrum of the x (CM_X, black line) and y (CM_Y, red line) components of the centre of mass of the specimen. The peaks in the spectrum correspond to the translation frequencies (ν_x, ν_y) of the specimen in the horizontal plane. A moving average algorithm was applied to the data (indicated by "MovAvg" in the legend) in order to smooth the lines for better readability.

The Fourier transform of the radii give the spectra of the oscillation frequencies. The problem is to identify the peaks of the oscillation modes to be able to apply the equations presented in Section 2.2. Using only the spectrum of a single radius, a clear distinct assignment of all expected oscillation peaks for $l = 2$, $m = 0, \pm1, \pm2$ (further denoted as $\nu_{2,0}$, $\nu_{2,\pm1}$, $\nu_{2,\pm2}$) is usually not possible (see Figure 3.5).

But by taking two arbitrary perpendicular radii (R_0, R_{90}) and building the sum (R_+) and difference (R_-) of them, one can show that certain oscillation frequencies in the according spectra of R_+ and R_- sum up or subtract to a constant value and thus vanish from the spectra. The $\nu_{2,0}$ oscillation mode vanishes in the R_- spectrum and the $\nu_{2,\pm2}$ oscillation mode does not show up in the R_+ spectrum any more. A mathematical proof of this is described in [12]. The only oscillation mode visible in both spectra should be $\nu_{2,\pm1}$ (see fig. 3.7).

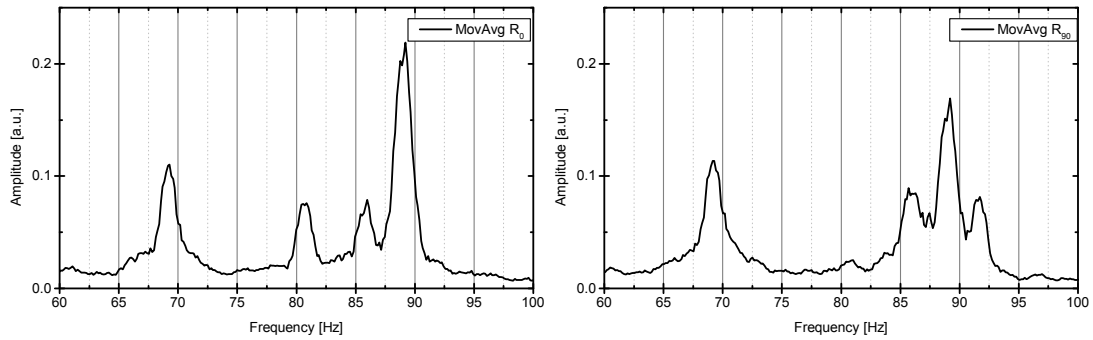

Figure 3.5: Comparison of the spectra of two perpendicular radii R_0 (left) and R_{90}(right). In each spectrum, only four of the five oscillation frequencies expected from the theory for $l = 2$ ($\nu_{2,0}$, $\nu_{2,\pm1}$, $\nu_{2,\pm2}$) are observable. For better readability, a moving average algorithm was applied to the data to smooth the lines.

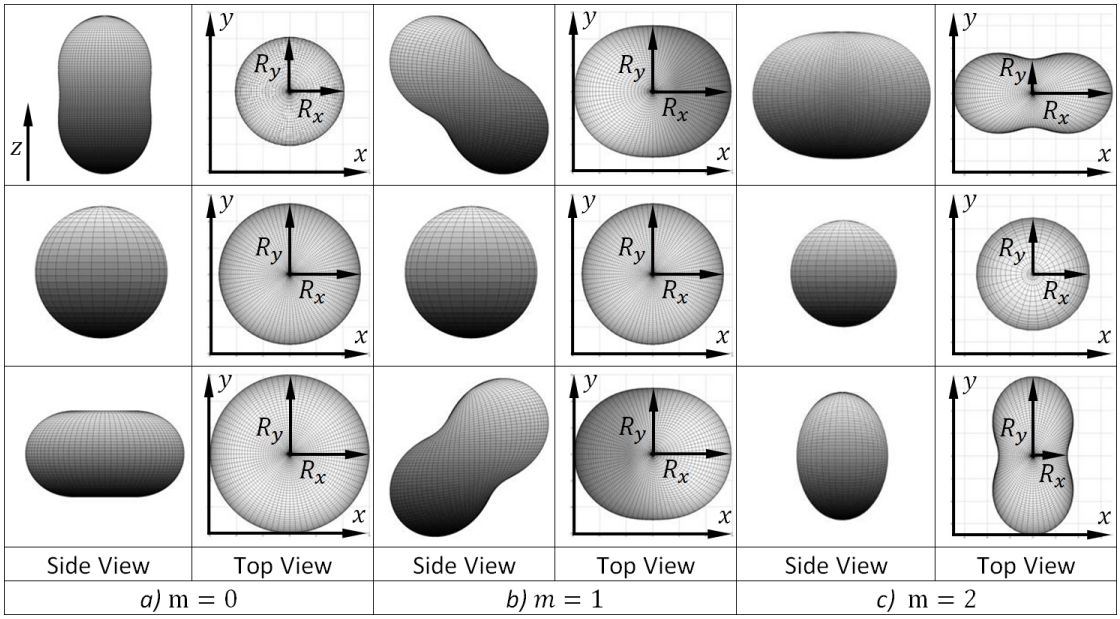

Figure 3.6: Oscillation modes for $l = 2$, $m = 0, \pm1, \pm2$. Looking at the evolution of the radii R_0 and R_{90} (here denoted as R_x and R_y) for each oscillation mode, the vanishing of oscillation modes in R_+ and R_- gets more vivid. In case of $m = 0$ it appears obvious that the difference of the perpendicular radii R_- will give a constant value near zero. For $m = 2$ it is plausible that the sum of the radii R_+ will add up to a constant value. Source of the image: [12]

Looking at the spectra of R_+ and R_- in Figure 3.7, one can see that the statements above hold true. The peaks can now be clearly assigned to the different oscillation modes. Another helpful rule for assigning the different oscillation modes is that the split of the oscillation frequencies due to the rotation of the specimen should be twice as large for the $m = \pm2$ modes than for the $m = \pm1$ modes (see Section 2.2).

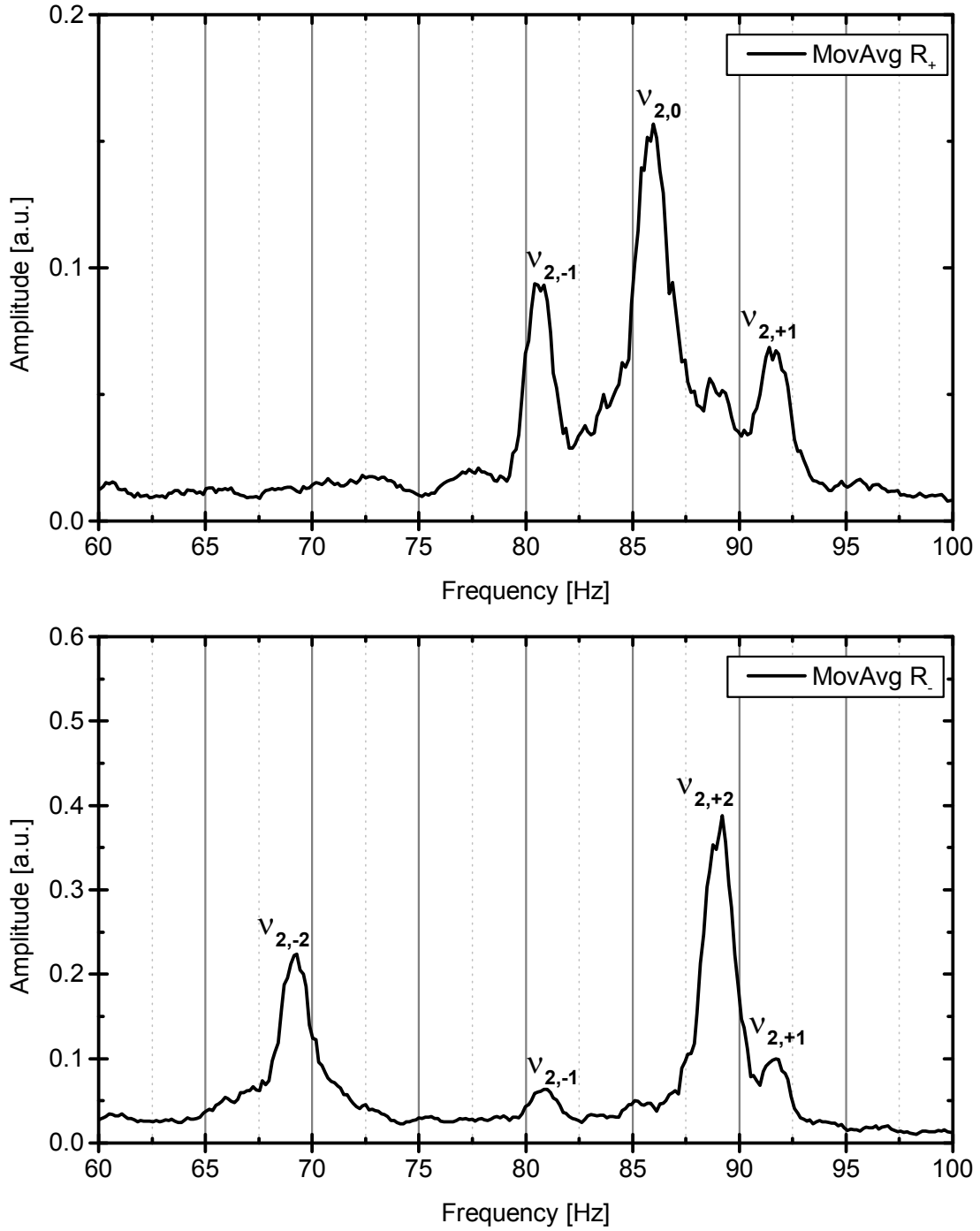

Figure 3.7: Comparison of the spectra of R_+ (top) and R_- (bottom). Since the peaks of $\nu_{2,\pm2}$ have to vanish in the spectrum of R_+, the one of $\nu_{2,0}$ has to vanish in R_- and $\nu_{2,\pm1}$ must be present in both spectra, the peaks and their respective frequencies in the spectra can be clearly assigned to the oscillation modes. Again, a moving average algorithm was applied to the data for better readability.

It must be said that the choice of the perpendicular radii to calculate R_+ and R_- is not completely arbitrary since the noise in the spectra may depend on the selected perpendicular radii. Thus, the choice of the radius R_0 and its perpendicular radius R_{90} was usually different for each temperature point. Since an image sequence of 4100 images at a frame rate of 600 fps results in a time frame of about 6.8 s, it was moreover sometimes inevitable to ignore data points in the beginning or at the end of the sequence if the levitation was slightly unstable during that time period. As a consequence, the frequency resolution is reduced in that case.

For each temperature point of each measurement, the spectra were analysed in the way described and the oscillation modes assigned. The surface tension was then calculated using the equations from Section 2.2 and the determined oscillation frequencies and the mass of the specimen as input.

As a side note, a new spectrum was introduced to the evaluation of the surface tension during this thesis (see Figure 3.8).

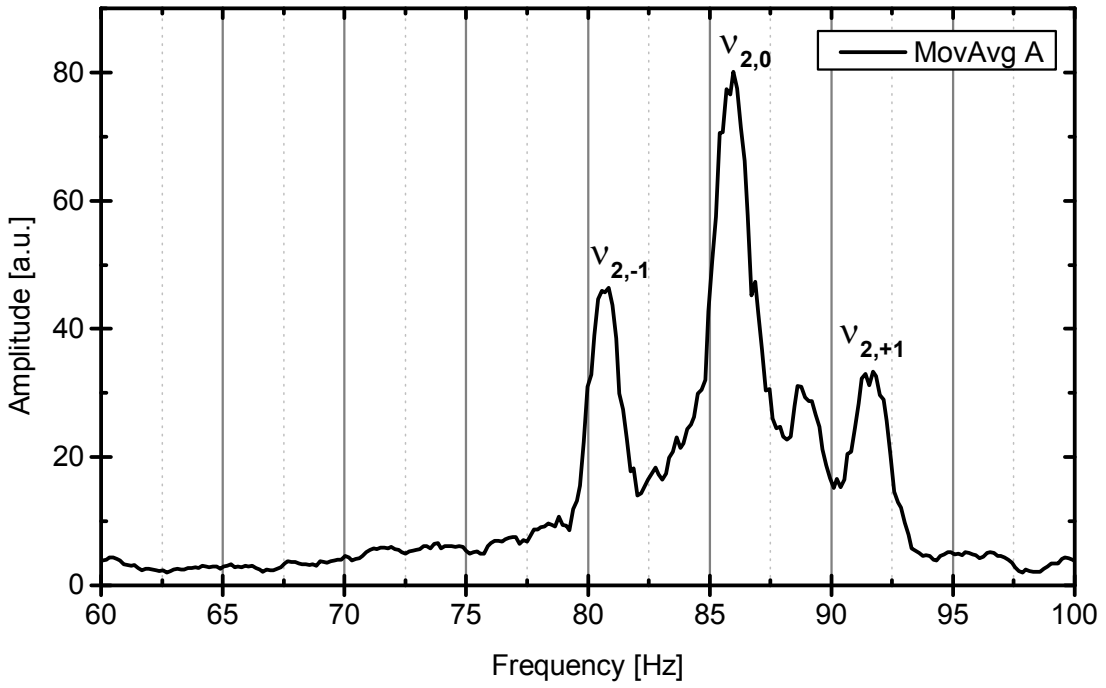

Figure 3.8: Fourier transform of the time evolution of the number of pixels in the image dedicated to the specimen as detected by the algorithm to determine the centre of mass (pixel intensity above threshold). The number of pixel is a measure for the area of the specimen. Without mathematical proof but qualitatively spoken, the oscillation modes contributing most to this spectrum should be the ones where the area in the top view changes significantly, namely $\nu_{2,0}$ and $\nu_{2,\pm1}$ (see Figure 3.6). This spectrum can possibly help to detect oscillation frequencies that may not be clearly visible in the other spectra. Again, a moving average algorithm was applied to smooth the lines in the spectrum for better readability.

Density evaluation

The density evaluation was done within a MATLAB script too. For each image (corresponding to a single line in the ASCII files), the radii were fitted with a Legendre polynomial up to the sixth order to have an analytic expression that represents the edge of the object (specimen or reference sphere respectively). Assuming a vertical axis symmetry, the volume of the object was calculated from the fitted Legendre polynomial (representing the projected area of the object). The final volume of the object was then calculated as the arithmetic mean value of all individual volumes. Due to the averaging of many pictures (4100 images) and thus a considerably large time period (approx. 34 s), the mean volume should quite well represent the actual volume of the specimen, although the projected area is highly fluctuating due to the oscillations of the specimen.

First, the data of the reference spheres were evaluated to determine the calibration factor between area in pixel and area in real metric units (e.g. m^2) as mentioned in Section 3.4. Then the volume of the specimen was evaluated for each temperature point and finally converted to a metric value using the calibration factor.

Using the calculated volume and the measured mass of the specimen, the specimen's density was calculated.

4 Results and Discussion

4.1 Challenging characteristics of aluminium

Some characteristics of aluminium had challenging effects on the measurement procedure and will be discussed in detail in this chapter. But first a list of aspects that simplified the measurements:

- No evaporation: As mentioned in Section 3.4, there was no noticeable evaporation of the sample material. This was most likely due to the fact that the maximum temperature reached (approx. 1550 K) was far below the boiling temperature of aluminium (approx. 2473 K).
- Stable levitation position: Regarding the stability of the levitation, aluminium proved to be a sample material quite easy to levitate. Even in case of larger displacements from the equilibrium position, the specimens stayed inside the high frequency field between the levitation coils.
  On the other hand, the amplitudes of the distortion from the equilibrium shape were quite sensitive to the size of the specimen, meaning bigger specimen showed larger oscillations and sometimes severe distortion. In this respect, smaller samples proved to behave better but limited the maximum temperature that could be reached (see the following points).

Beside those beneficial properties, some characteristics of aluminium complicated a precise measurement of surface tension and density using the electromagnetic levitation method:

Affinity to oxygen

Clean aluminium exposed to air instantaneously builds a layer of aluminium oxide (Al_2O_3, called "alumina") with a thickness in the range of a few nanometres [13]. In order to investigate a "clean" aluminium specimen, not only the oxide layer has to be removed from the surface (e.g. by polishing or chemical reaction) but also the transfer of the specimen from the preparation facility to the probe chamber has to be done in an oxygen-free environment, requiring a vacuum transfer chamber or similar setup.

But even if an oxygen-free surface can be achieved with the mentioned effort, there is the possibility that the bulk of the specimen has contaminations of aluminium oxide that may come to the surface as the specimen liquefies during the electromagnetic levitation experiment (and certainly will due to the stirring effects described in Section 2.1). Thus, the only way to achieve a completely oxygen-free sample material is to "clean" it inside the probe chamber during the experiment itself. This approach needs a sophisticated experimental setup in order to absorb the free oxygen from the atmosphere inside the probe chamber as well as achieve high specimen temperatures to get rid of the aluminium oxide already built.

The electromagnetic levitation setup at TU Graz was not (yet) equipped with an according device to control or measure the oxygen partial pressure of the atmosphere in the probe chamber, thus all measurements have to be regarded as oxygen contaminated. Nevertheless, much effort was spend during the measurements described in this thesis to reduce the oxygen in the probe chamber to the lowest possible level. As a consequence, the measured surface tension of the specimen is lowered in the presence of aluminium oxide compared to an oxygen - free specimen (this will be discussed in Section 4.2 in more detail).

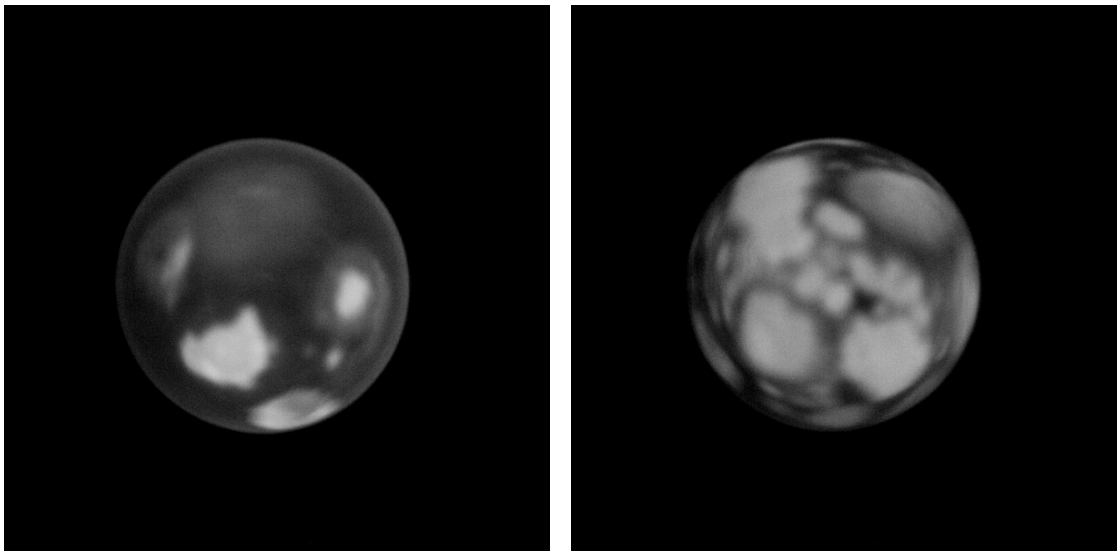

Figure 4.1: Images of aluminium oxide on the specimen surface (left: 1014 K, right: 981 K). A gamma correction was applied to both images in order to increase the contrast on paper when printed.

Since aluminium oxide has a significant higher melting point (2345 K) than aluminium (933 K), "islands" of solid aluminium oxide remained on the surface of the specimen when the bulk aluminium was liquefied. Those "islands" of aluminium oxide do not only affect the surface tension of the specimen but also complicate the temperature

measurement due to the higher spectral emissivity of the oxide resulting in a higher apparent temperature of the specimen surface. As a consequence, the latter effect added more noise to the temperature signal of the pyrometer the more the surface was covered with those moving "islands" of aluminium oxide.

By pushing the limits of operation regarding the minimum pressure inside the probe chamber (see Section 3.2) down to 300 mbar and even lower (depending on specimen size), it was possible to heat the specimen up to almost 1550 K. Levitating the specimen at those elevated temperatures for time periods of several minutes achieved the oxide to disappear from the specimen surface. The process behind this phenomenon was most likely the reduction of solid aluminium oxide (solid, Al_2O_3) to aluminium (liquid, Al) and water vapour (gaseous, H_2O) by the hydrogen (gaseous, H_2) enriched atmosphere:

$$Al_2O_3(s) + 3H_2(g) \longleftrightarrow 2Al(l) + 3H_2O(g). \tag{4.1}$$

Since the apparatus was not equipped with any device to measure the partial pressures of oxygen, hydrogen or the partial vapour pressure, this assumption can not be proved. But there is evidence in literature where similar processes were experimentally observed. The equilibrium diagram for the system Al-Al_2O_3 (see Figure 4.2) seems to support this thesis too. Both, elevated temperature and a low ratio of partial vapour pressure (due to the evacuation of the specimen chamber) to hydrogen partial pressure shift the reactions equilibrium towards the reduction of aluminium oxide to liquid aluminium.

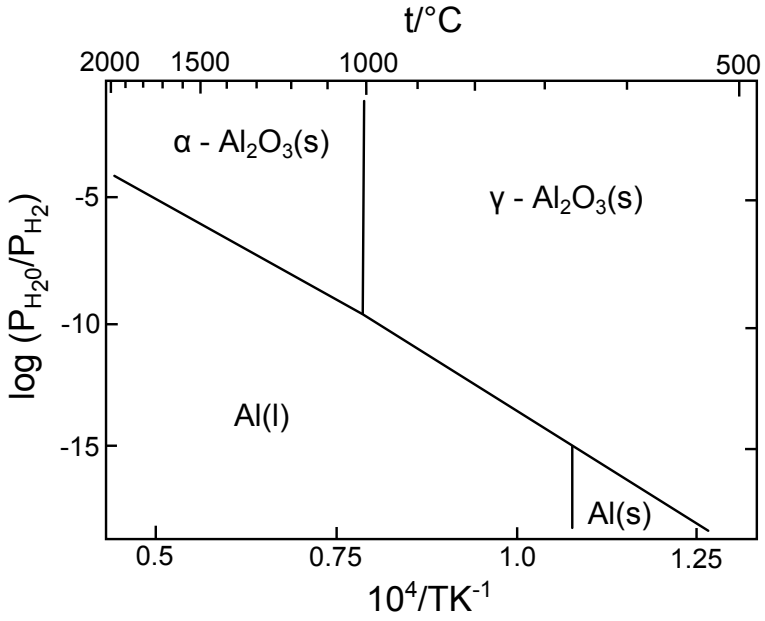

Figure 4.2: Al-Al_2O_3 equilibrium diagram as a function of temperature and different ratios of H_2O to H_2. Redrawn after: [14].

When the specimen was cooled down during the measurement, the aluminium oxide again built up on the surface with time (either due to lower stirring at lower temperatures or by chemical reaction). The lower the temperature and the longer the specimen was levitated, the more oxide built on the surface until almost the complete surface was covered with a solid oxide layer. As a consequence, the measurement had to be aborted at a certain point, not only because the surface tension was most likely to be affected heavily by the oxide layer but also because the measurement of temperature was no longer possible. Oxide layers that almost fully cover the specimens surface turned out to be very solid so that even a repeated heating procedure by exchanging the gas atmosphere from He + H_2 back to Ar + H_2 did not achieve a visible melting of the specimen any more. One reason for this is certainly the higher emissivity of the specimen surface when covered by an oxide layer which results in a higher heat dissipation from the surface of the specimen by thermal radiation. However, the eddy currents heating the specimen by ohmic losses are limited by the maximum power output of the high frequency generator at the same time. Therefore, the temperature needed to get rid of the oxide layer is no longer reachable and the melting of the aluminium beneath the oxide layer is not visible.

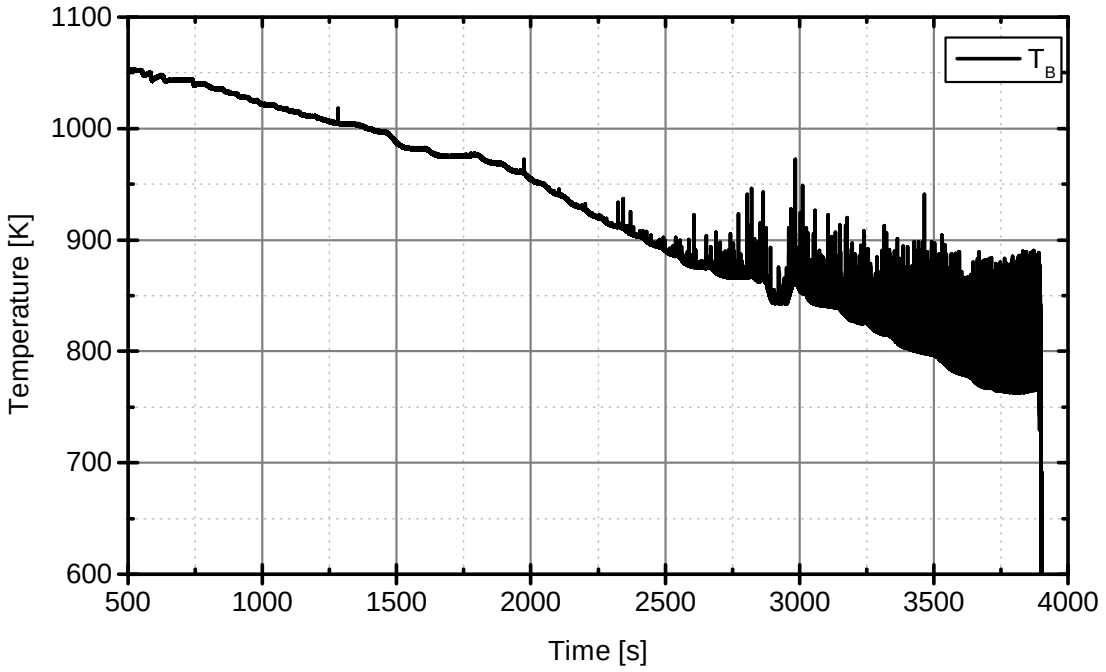

Figure 4.3: Record of the "black temperature" during a measurement. When the specimen is cooled down, the oxide again builds up on the surface of the specimen and adds severe noise to the temperature signal.

The only way to bypass this phenomenon was to perform the measurements quickly, especially at lower temperatures in order to finish the measurement before too much aluminium oxide could be build up.

Low melting point

For industrial applications such as metal processing, thermophysical properties over a broad temperature range in general but especially near the melting point are of interest. Aluminium however has a low melting point (933 K) when compared to other metals and thus shows a low thermal radiation in the visible spectrum of light at this temperature (see Figure 4.4).

This is a severe problem for the evaluation of the surface tension since the method depends on (direct) images of the thermal radiation of the levitated specimen. The low thermal radiation at temperatures at the melting point and slightly above results in a very bad contrast of the image. As a consequence, the specimen in the image can not be distinguished from the dark background any more. For the density evaluation, this is not a problem at all since shadowgraphs are recorded in this case.

In order to obtain images of the specimen at temperatures as close as possible to the melting temperature, the experimental parameters of the imaging system were fine tuned. Since the recorded intensity is proportional to the shutter time of the camera, this is the first in a series of parameters to adjust in order to improve the contrast of the images. But the shutter time has a principal limit regarding the lowest possible value, which is determined by the recording rate. By lowering the recording rate down to 200 fps, it was possible to achieve shutter times up to 5 ms. The camera would allow even lower frame rates but due to the Nyquist-Shannon sampling theorem [15], the sampling frequency has to be two times larger than the frequency of the signal to be reconstructed. Since the frequencies of the surface oscillations of interest observed in the spectra reached almost 95 Hz (see Section 3.5), a minimum frame rate of 200 Hz was a reasonable value in order to fulfil the Nyquist-Shannon sampling theorem.

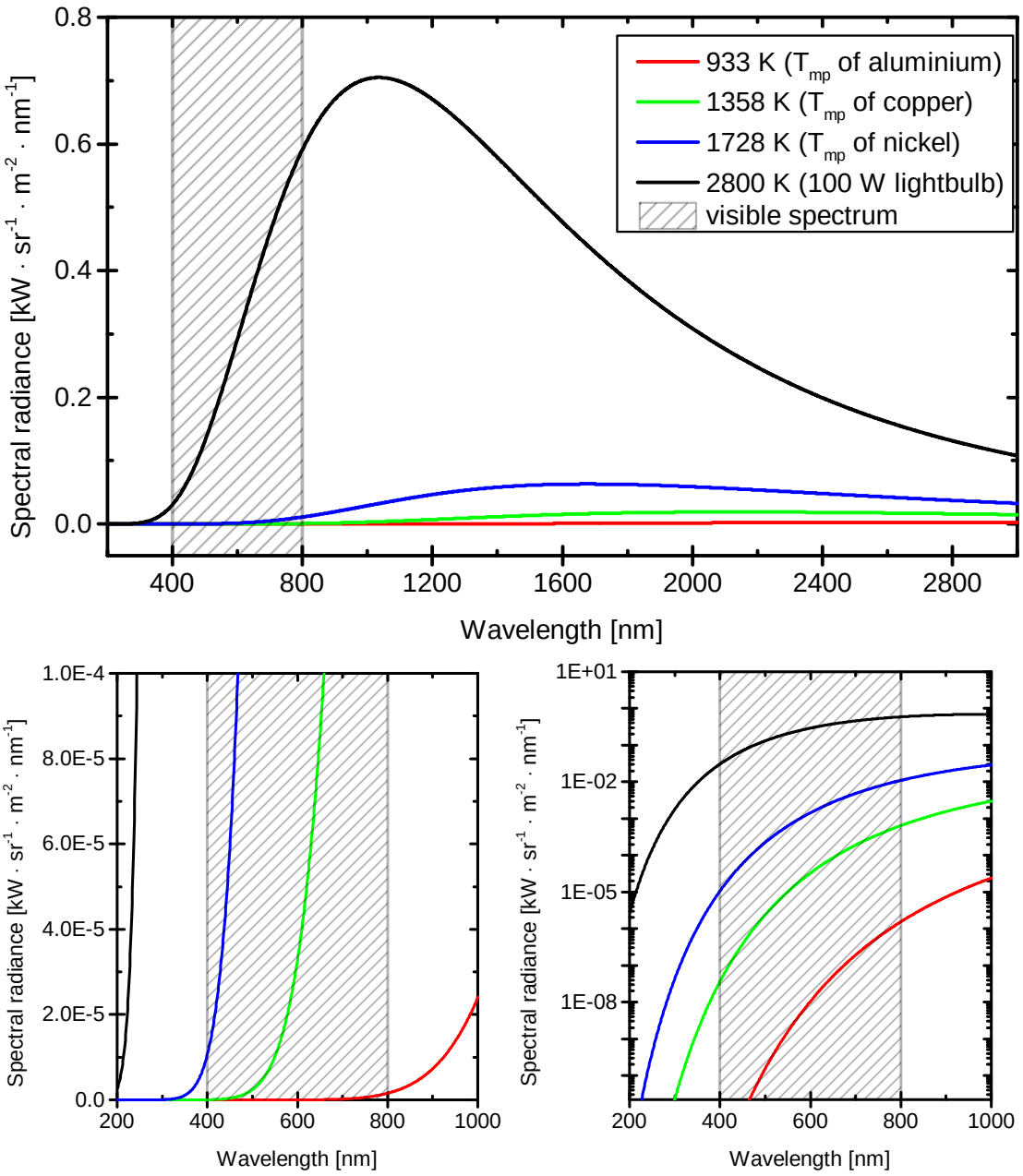

Figure 4.4: Spectral radiance of a "black body" as a function of wavelength for different temperatures (top). For comparison, the melting point of the sample material investigated (aluminium, red line) is depicted together with the melting points of other metals (green line: copper, blue line: nickel) are displayed. As a reference, the spectral radiance of a 100 W light bulb (black line) is also shown. The wavelength range of the visible spectrum is illustrated as the shaded area. The bottom-left figure shows a magnified area of the spectral radiance to illustrate the low thermal radiation in the visible spectrum at the melting temperature of aluminium compared to other temperatures. Bottom-right: The same detail is shown with logarithmic scale for the spectral radiance to clearly depict this difference and its orders of magnitude.

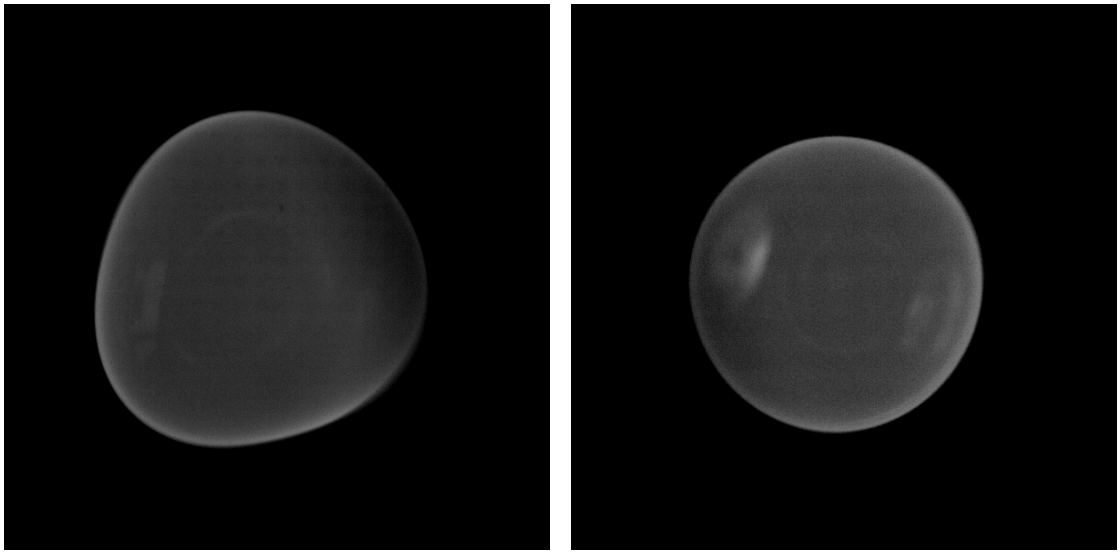

Figure 4.5: Comparison of thermal radiation with different settings for frame rate and shutter time. Left: Image of the specimen at 1274 K with "standard" settings (frame rate: 600 fps, shutter time: 1.5 ms). Right: Image of the specimen at 1091 K using improved settings (400 fps, 2.5 ms) and a optimized optical setup. Although recorded at lower temperature ($\Delta T \approx 180\,\mathrm{K}$), the image still gives contrast that can be evaluated by the software. The same gamma correction was applied to both images in order to increase the contrast on paper when printed.

The problem with lowering the shutter time is the reduced sharpness of the edges of the specimen, the images get blurry due to the movement of the specimen during the exposure of the camera chip. As a consequence, the peaks of the different oscillation modes are harder to recognise in the spectrum due to the higher background and lower signal to noise ratio respectively.

During this thesis it was possible to record images for the surface tension evaluation almost (81 ± 21) K close to the melting point by fine tuning the parameters of the imaging system as described above. Unfortunately, it was not possible to evaluate images closer to the melting temperature of aluminium or even for slight undercooling of the specimen (as this has been achieved for other sample materials in the past by Aziz et al. [12, 16]).

Low heating

Aluminium has a high electrical conductivity of $37.7 \cdot 10^6\,\mathrm{A \cdot V^{-1} \cdot m^{-1}}$ and is ranked fourth regarding this property after silver, copper and gold [17]. Since the ohmic losses of the induced eddy currents are the source of the heating of the specimen in the electromagnetic levitation setup, aluminium can be less efficiently heated using the same specimen volume compared to other sample materials.

Due to the restrictions of the minimum pressure of the atmosphere in the probe chamber

($> 200\,\mathrm{mbar}$, see Section 3.2) and the limitation of maximum power output of the high frequency generator, the maximum temperature reached during all experiments of this thesis was approx. 1550 K. The measured data points between $(1014 \pm 21 - 1550 \pm 43)\,\mathrm{K}$ already represent a reasonable temperature range for electromagnetic levitation experiments, however, additional data at higher temperatures would have been interesting in order to improve the quality of the linear fit of the data presented in Section 4.2.

Moreover, the maximum temperature that could be reached was strongly depending on the specimen size or volume respectively. This can be explained by simple geometry considerations: The volume of the specimen in the liquid phase, where the flux of the electromagnetic field passes and eddy currents are induced, is the volume of an (almost) perfect sphere, thus proportional to the third order (r^3) of the radius or diameter respectively. But the surface of the sphere, which is the fundamental interface for the heat dissipation (convection and thermal radiation) is only proportional to the radius/diameter to the second order r^2. Thus, bigger specimen could be heated more "efficiently" but at the same time, larger deformations from the equilibrium shape and their difficult evaluation (less concise peaks in the spectrum) had to be accepted.

4.2 Results

Introductory comments

During this thesis, several different sized specimen of the sample material aluminium were investigated. But only specimen that fulfilled a complete measurement cycle including weighing after the experiment are included in this results section. Specimen that were not savely caught with the sample holder after the experiment or completely lost during the experiment were discarded from further analysis since it can not be proven for those specimen that no sample material evaporated during the measurement.

The specimen of the surface tension measurements were not identical to the specimen of the density measurements, as a brief look on the different specimen masses reveals. This has two reasons:

- The image recording software neither did allow to record images simultaneously of the top and side camera nor to simply switch between those two cameras without larger configuration expenses. Whereas the first point is still a feature of interest and planned to be realized in the future, the image recording software was extended with the feature to quickly switch between the two cameras towards the end of this thesis.
- As elaborated in Section 4.1, it was not possible to heat the specimens again to the liquid phase after a completed measurement cycle. As a consequence, it was not possible to repeat a measurement with the same specimen in order to perform the density measurement after the surface tension measurement or vice versa.

Surface tension measurement

During the surface tension measurement runs, the following specimen were investigated:

Table 4.1: Table of the specimen and their mass that were investigated during the surface tension measurements.

Nr.	...	Specimen number
m_S	...	Specimen mass at start of experiment (± 0.1 mg)
m_E	...	Specimen mass at end of experiment (± 0.1 mg)
Δm	...	Loss of mass during the experiment (± 0.2 mg)

Nr.	m_S [mg]	m_E [mg]	Δm [mg]
1	122.6	122.6	0.0
2	133.6	133.6	0.0
3	137.6	137.6	0.0
4	135.2	135.2	0.0
5[1]	106.6	106.5	0.1
6	110.8	110.6	0.2

Figure 4.6 shows the results of the surface tension measurements of aluminium. A satisfying detail is that the surface tension obtained at same temperatures coincides for different specimens or specimen masses respectively. Accordingly the oscillation frequencies showed a dependence of the specimen mass like proposed by the theory (see Section 2.2). The fine tune of the image recording parameters during this thesis as described in Section 4.1 is also clearly visible as the temperature range covered is subsequently extended towards lower temperatures. As elaborated in Section 4.1, no measured data closer than (1014 ± 21) K to the melting point could be obtained due to the low thermal radiation. Sections 5.2 and 5.1 will elaborate on the source of the uncertainties in more detail.

The surface tension appears to decrease linearly with temperature in the liquid phase. A linear fit was applied to all data points according to the following model:

$$\gamma_l = \gamma_{mp} + \frac{d\gamma}{dT} \cdot (T - T_{mp}) \tag{4.2}$$

[1] This is the same specimen as specimen nr. 5 of the density measurement since from that date on, the image recording software was extended by the ability to quickly switch between the two cameras.

with:

γ_l ... surface tension in the liquid phase

γ_{mp} ... surface tension at melting point

$\frac{d\gamma}{dT}$ ... change of surface tension with temperature

T_{mp} ... Temperature at melting point (933 K).

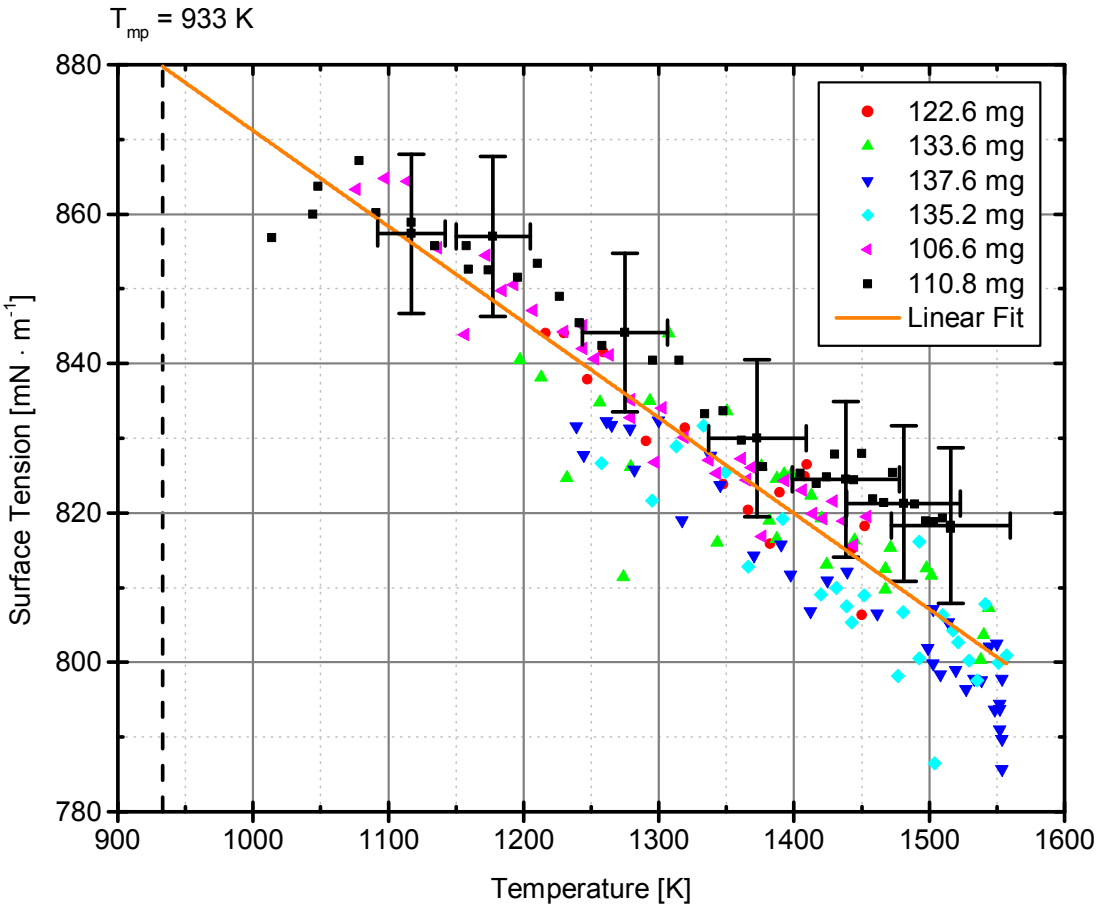

Figure 4.6: Results of the surface tension measurements. For better readability, the uncertainty bars are plotted only for one single measurement and only for every fifth data point.

The fit parameters obtained by the least squares fit are:

$$\gamma_{mp} = (880 \pm 2)\,\mathrm{mN \cdot m^{-1}} \tag{4.3}$$

$$\frac{d\gamma}{dT} = -(0.128 \pm 0.004)\,\mathrm{mN \cdot m^{-1} \cdot K^{-1}} \tag{4.4}$$

In Figure 4.7 the obtained linear fit for the measurement data is compared to the linear

fits of other surface tension measurements available in literature (see Table 4.2). It must be stated that the surface tension data in literature already significantly varies, not only the value of γ_{mp} but also the value of $d\gamma/dT$, depending on the measurement method and the (claimed) specimen condition (oxygen - free or not). Especially the differences in the value of $d\gamma/dT$ are interesting since this indicates a significant different temperature behaviour of the specimen.

The figure illustrates that the data obtained shows a satisfying agreement with the more recent literature values, especially with the ones obtained by Brillo et al. [18] using electromagnetic levitation too.

Table 4.2: Reference values for the surface tension at the melting point γ_{mp} and the change of surface tension with temperature $\frac{d\gamma}{dT}$ from various publications. The measurement method abbreviations are: EML... Electromagnetic Levitation, MBP... Maximum Bubble Pressure , SD... Sessile Drop, LD... Large Drop, R... recommended literature values.

Author / Group	**Method**	**Year**	γ_{mp} $[\mathbf{mN{\cdot}m^{-1}}]$	$\frac{d\gamma}{dT}$ $[\mathbf{mN{\cdot}m^{-1}\cdot K^{-1}}]$
Brillo et al. [18]	EML	2016	866 ± 30	-0.146 ± 0.04
Kobatake et al. [19]	EML	2015	979 ± 50	-0.271 ± 0.0218
Molina et al. [20]	LD	2007	955	-0.24
Mills et al. [21]	R	2002	871	-0.155
Eustathopolous [22]	SD	1999	867	-0.15
Pamies et al. [23]	MBP	1984	873[2]	-0.12
Goumiri et al. [24]	SD	1979	865	-0.12
Laty et al. [25]	SD	1977	865 ± 6	-0.15
Popel et al. [26]	SD	1975	930	-0.146
This work	**EML**	**2016**	880 ± 2	-0.128 ± 0.004

[2]Classified as oxidized by the author.

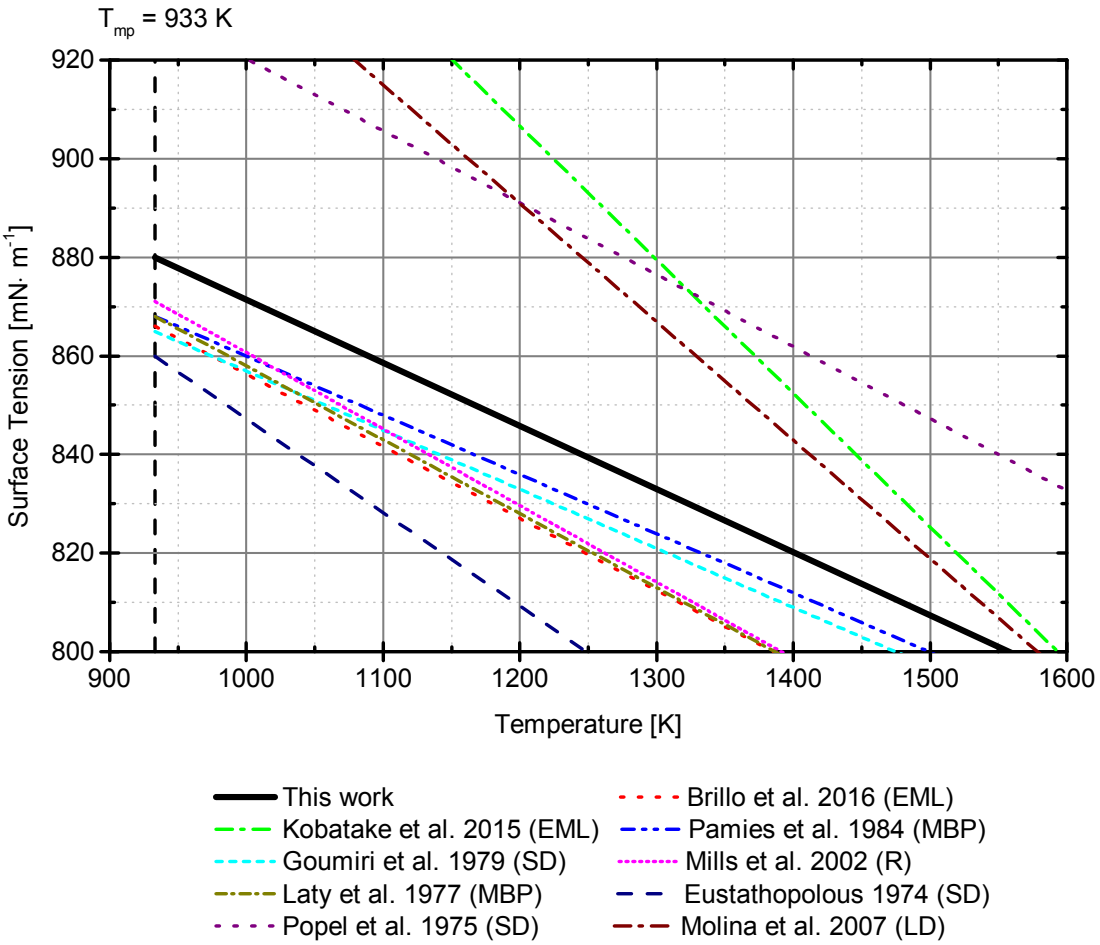

Figure 4.7: Comparison of the surface tension measurements with reference data from different literature sources (see Table 4.2). There is a good agreement of the measured data with the literature values concerning the change of surface tension with temperature $d\gamma/dT$, whereas the surface tension at the melting temperature γ_{mp} appears a bit offset. This value varies (partly) significantly for the different literature sources. Beside the possible influence of the measurement method itself, the most probable reason for the slight offset of the different lines is the oxygen/oxide contamination of the specimen. This is supported by the data of [19, 20] who have performed the measurements under strongly oxygen-reduced conditions and without oxide on the specimen surface. Those measurements show a significantly larger surface tension value at the melting point γ_{mp}. Moreover the change in surface tension with temperature is completely different.

Results of density measurement

The following table lists all specimen and their mass that were investigated during the density measurements:

Table 4.3: Table of the specimen and their mass that were investigated during the surface tension measurements:

Nr.	...	Specimen number
m_S	...	Specimen mass at start of experiment (± 0.1 mg)
m_E	...	Specimen mass at end of experiment (± 0.1 mg)
Δm	...	Loss of mass during the experiment (± 0.2 mg)

Nr.	m_S [mg]	m_E [mg]	Δm [mg]
1	120.2	120.1	0.1
2[3]	125.6	125.5	0.1
3[3]	113.1	113.1	0.0
4	107.7	107.7	0.0
5[4]	106.6	106.5	0.1
6	111.5	111.3	0.2

The results of the density measurements of aluminium are presented in Figure 4.8. Again, the density obtained at same temperatures coincides for different specimens like proposed by the theory. Contrary to the surface tension measurement, acquisition of data points at the melting point and even at slight undercooling down to (903 ± 16) K could be achieved due to the image recording process based on shadowgraphs instead of images of thermal radiation (as elaborated in Section 3.4). Nevertheless, the scatter of the data points appears quite strong and also different for each specimen. A possible explanation will be given in Section 5.2.

The uncertainty bars are again plotted only for one single measurement for better readability. A noticeable detail is the size of the error bars, which seem small compared to the overall scatter of the data. This is contrary to the plot of the surface tension data, where the scatter of the data is within the range of the error bars. This phenomenon and the source of the uncertainties will be discussed in Section 5.2 in more detail.

[3] Those measurements were performed by a group of students during a laboratory exercise under supervision of Dr. Kirmanj Aziz.

[4] This is the same specimen as specimen nr. 5 of the surface tension measurement since from that date on, the image recording software was extended by the ability to quickly switch between the two cameras.

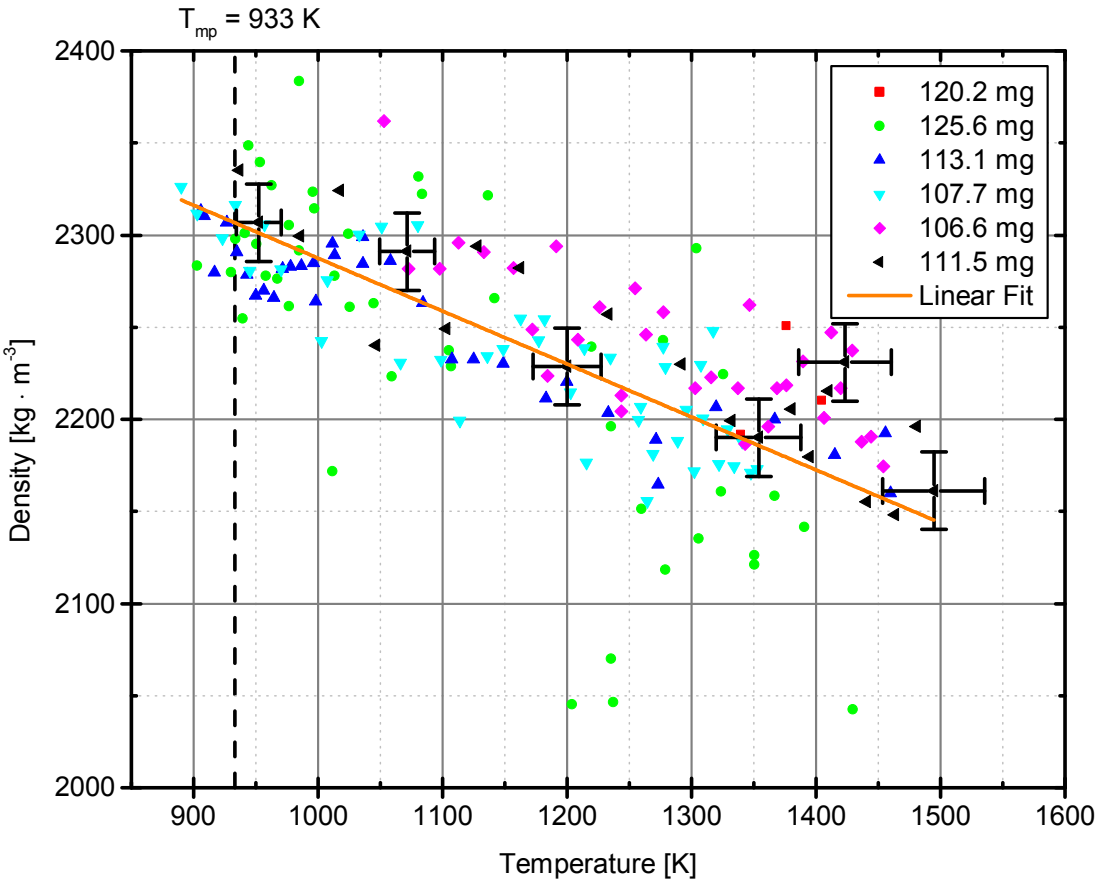

Figure 4.8: Results of the density measurements. For better readability, the uncertainty bars are plotted only for one single measurement and only for every third data point.

For the change of density with temperature, also a linear behaviour with negative slope was assumed. The linear fit applied to all data points follows the linear model for the temperature dependence of the density in the liquid phase ρ_l:

$$\rho_l = \rho_{mp} + \frac{d\rho}{dT} \cdot (T - T_{mp}) \tag{4.5}$$

with:

ρ_l ... density in the liquid phase

ρ_{mp} ... density at melting point

$\frac{d\rho}{dT}$ ... change of density with temperature

T_{mp} ... Temperature at melting point (933 K).

Using a least squares fit method, the following fit parameters were obtained:

$$\rho_{mp} = (2307 \pm 8)\,\mathrm{kg \cdot m^{-3}} \tag{4.6}$$

$$\frac{d\rho_l}{dT} = -(0.29 \pm 0.03)\,\mathrm{kg \cdot m^{-3} \cdot K^{-1}}. \tag{4.7}$$

The linear fit obtained for the measurement data is compared in Figure 4.9 to linear fits of other density measurements available in literature (see Table 4.4). Similar to the comparison of the surface tension data, the values in literature for both, density at the melting point ρ_{mp} and change of density with temperature $d\rho_l/dT$, also vary significantly. This is somewhat surprising since the density should be less affected by the condition of the specimen (oxide content) than the surface tension and thus a better coincidence of the values in literature would have been likely to expect for the density data. Beside the possible influence of the applied measurement methods on the obtained values, also a discrepancy for the data obtained by electromagnetic levitation can be observed [27, 28].

The value of the change of density with temperature ($d\rho_l/dT$) obtained within this thesis agrees quite well with the values from literature, whereas the value of the density at the melting point (ρ_{mp}) appears a bit offset in this comparison. But a recent publication of Peng et al. [29], where (amongst others) the density of pure aluminium was investigated by using the electromagnetic levitation technique, shows a good agreement with the measured data of this thesis. Unfortunately, the authors of this publication do not provide reference values from literature and therefore a discussion about the possible reasons for this discrepancy is missing.

Nevertheless, there is the problem inherent to the measurement method, that the volume determined by the evaluation algorithms may be systematically lower or higher than the real volume. This is a consequence of the assumptions made, e.g. vertical rotation symmetry of the specimen, small deformations from the equilibrium shape and of the image evaluation algorithms.

Table 4.4: Reference values for the density at the melting point ρ_{mp} and the change of density with temperature $\frac{d\rho}{dT}$ from various publications. The measurement method abbreviations are: EML... Electromagnetic Levitation, G... Gamma Attenuation, R... recommended literature values.

Author / Group	**Method**	**Year**	ρ_{mp} $[\mathbf{kg{\cdot}m^{-3}}]$	$\frac{d\rho}{dT}$ $[\mathbf{kg{\cdot}m^{-3}\cdot K^{-1}}]$
Peng et al. [29]	EML	2015	2290	-0.251
Iida et al. [30]	R	2015	2385	-0.35
Schmitz et al. [27]	EML	2012	2360 ± 10	-0.30 ± 0.1
Brillo et al. [28]	EML	2008	2350	-0.2
Assael et al. [31]	R	2006	2377	-0.31
Mills et al. [21]	R	2002	2380	-0.35
Smith et al. [32]	G	1999	2368	-0.264
Nasch et al. [33]	G	1995	2375	-0.233
This work	**EML**	**2016**	2307 ± 8	-0.29 ± 0.03

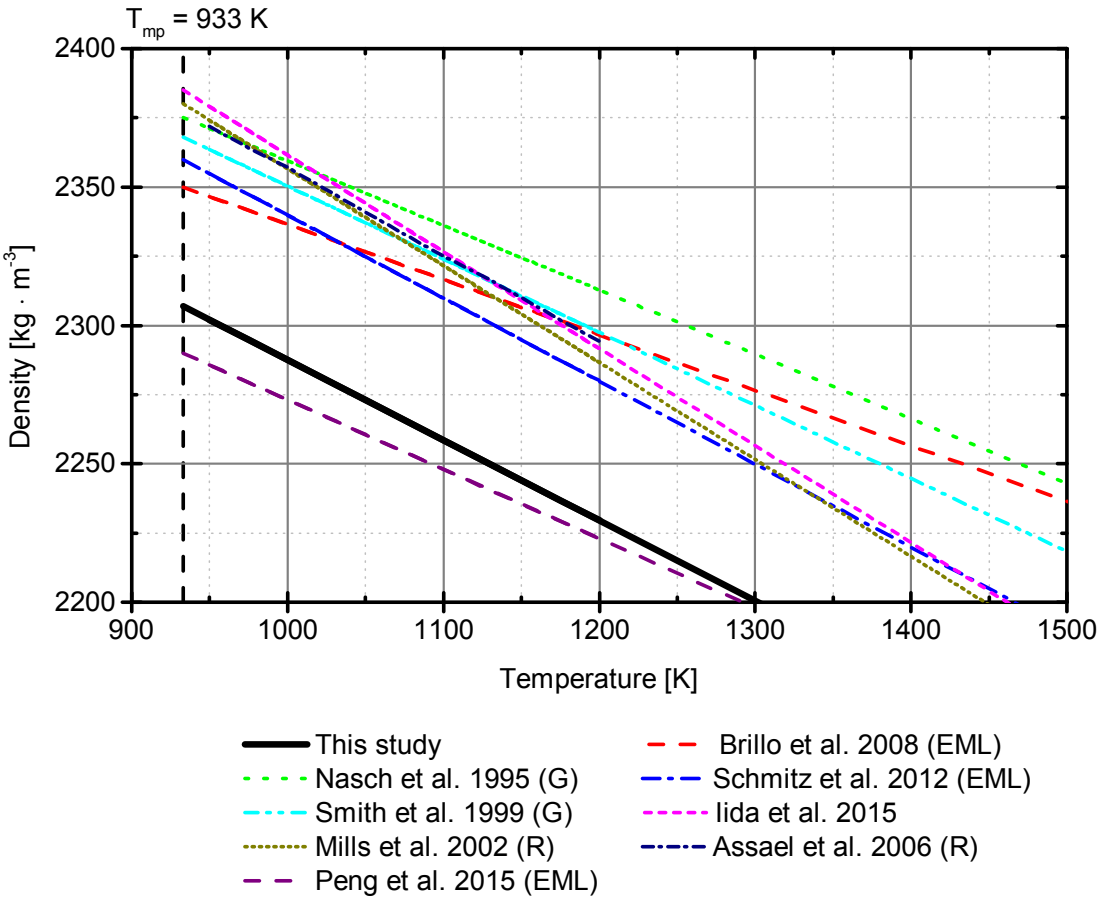

Figure 4.9: Comparison of the density measurements with reference data from different literature sources (see Table 4.4). Concerning the change of density with temperature $d\rho_l/dT$, there is a good agreement of the measured data with the literature values whereas the density at the melting temperature ρ_{mp} is definitely offset, although it appears to coincide with the data published by Peng et al. in 2015 [29], who used the electromagnetic levitation technique too. The offset of the measured data is most probably due to a systematic overestimation of the actual specimen volume, a problem inherent to the measurement method and the assumptions or approximations made within the data evaluation. This would explain why the change of density with temperature shows nevertheless a good agreement with the reference data.

5 Uncertainty Analysis

The uncertainties of each single measurement value were evaluated according to GUM[1] . Section 5.2 will deal with the different aspects of the uncertainty budget for both, surface tension and density evaluation in more detail. But as already elaborated in Section 4.1, the contact-less temperature measurement of the levitated aluminium specimens via thermal radiation thermometry (pyrometer) was a very challenging task. This is why this chapter will first of all discuss the uncertainty in temperature measurement and its consequences.

5.1 Uncertainty of temperature

In various publications (e.g. [34, 3, 4]) in this field, the uncertainty of the measured temperatures was (roughly) estimated to be $\Delta T \approx 10\,\mathrm{K}$ over the whole temperature measurement range. But regarding the very special characteristics of aluminium concerning the temperature measurement (aluminium oxide), a more detailed and sophisticated discussion of this topic appears to be appropriate.

As discussed in Section 3.3, the temperature readings during these measurements correspond to the "black temperature" T_B of the specimen as the pyrometer is configured to a spectral emissivity of $\varepsilon = 1$. The real temperature of the specimen is recalculated after the experiment from those temperature readings by using Equation 3.2

$$T = \left(\frac{1}{T_B} + \frac{k \cdot \lambda}{c \cdot h} \ln(\varepsilon) \right)^{-1} \tag{3.2}$$

and the real emissivity of the specimen surface calibrated at the solidification plateau according to Equation 3.1

$$\varepsilon = \exp\left(\frac{c \cdot h}{k \cdot \lambda} \left(\frac{1}{T} - \frac{1}{T_B} \right) \right). \tag{3.1}$$

The physical constants as well as the true temperature T of the melting/solidification point of the sample material is assumed to be known with good precision from the

[1] Guide to the Expression of Uncertainty in Measurement, see `http://www.bipm.org/en/publications/guides/gum.html`

literature and thus free of uncertainty. In both cases, the "black temperature" reading T_B is the experimental observable afflicted by a measurement uncertainty.

Within this discussion of the temperature uncertainty, we'll distinguish between the black temperature reading T_B at the calibration point used in Equation 3.1 (further denoted as $T_{B,Calibr.}$) and the black temperature reading during the measurement T_B as used in Equation 3.2 (further denoted as $T_{B,Meas.}$). This can be argued as followed:

- The solidification plateau as illustrated in Figure 3.1 was usually not that clearly visible after a full measurement run due to the noise in the temperature signal caused by the aluminium oxide (see Section 4.1). It is appropriate to estimate the uncertainty of the "black temperature" reading of the solidification plateau to a minimum of $\Delta T_{B,Calibr.} = 10\,\mathrm{K}$.
- The "black temperature" reading during the measurement was usually quite clear although it got more and more noisy while the specimen was cooled down (see Section 4.1 and Figure 4.3). The overall uncertainty of the "black temperature" reading $T_{B,Meas.}$ was thus roughly estimated to be $\Delta T_{B,Meas.} = 5\,\mathrm{K}$.

According to the rules of GUM, the combined standard uncertainty u_c for the quantity of interest calculated by a model equation $y = f(x_i)$ is expressed by the positive square root of the combined variance ${u_c}^2(y)$, given by [35]

$$ {u_c}^2(y) = \sum_{i=1}^{N} \left(\frac{\partial f}{\partial x_i} \right)^2 u^2(x_i). \tag{5.1} $$

This equation is only valid for uncorrelated (independent) input quantities and $u(x_i)$ is the standard uncertainty of the individual input quantities. Remembering the formulas how to recalculate the true temperature from the "black temperature" readings from Section 3.3

$$ \varepsilon = \exp\left(\frac{c \cdot h}{k \cdot \lambda} \left(\frac{1}{T} - \frac{1}{T_{B,Calibr.}} \right) \right) \tag{3.1} $$

$$ T = \left(\frac{1}{T_{B,Meas.}} + \frac{k \cdot \lambda}{c \cdot h} \ln(\varepsilon) \right)^{-1} \tag{3.2} $$

the standard uncertainty of the recalculated temperatures $u_c(T)$ (further denoted as ΔT) can be expressed by the formula following the rules of error propagation

$$ \begin{aligned} \Delta T &= \sqrt{ \left(\frac{\partial T}{\partial T_{B,Meas.}} \cdot \Delta T_{B,Meas.} \right)^2 + \left(\frac{\partial T}{\partial \varepsilon} \cdot \Delta \varepsilon \right)^2 } \\ &= \sqrt{ \left(\frac{\partial T}{\partial T_{B,Meas.}} \cdot \Delta T_{B,Meas.} \right)^2 + \left(\frac{\partial T}{\partial \varepsilon} \cdot \frac{\partial \varepsilon}{\partial T_{B,Calibr.}} \Delta T_{B,Calibr.} \right)^2 } \end{aligned} \tag{5.2} $$

with the uncertainty contributions to the true temperature due to $\Delta T_{B,Meas.}$ and $\Delta T_{B,Calibr.}$

$$\frac{\partial T}{\partial T_{B,Meas.}} \cdot \Delta T_{B,Meas.} \ldots \text{contribution of } \Delta T_{B,Meas.}$$
$$\frac{\partial T}{\partial \varepsilon} \cdot \frac{\partial \varepsilon}{\partial T_{B,Calibr.}} \cdot \Delta T_{B,Calibr.} \ldots \text{contribution of } \Delta T_{B,Calibr.}$$

Each contribution can be expressed analytically by building the partial derivatives in respect to $T_{B,Meas.}$ and $T_{B,Calibr.}$ of the Equations 3.2 and 3.1

- Uncertainty contribution to the true temperature due to $\Delta T_{B,Meas.}$:

$$\begin{aligned}\frac{\partial T}{\partial T_{B,Meas.}} &= (-1) \cdot \left(\frac{1}{T_B} + \frac{k \cdot \lambda}{c \cdot h} \ln(\varepsilon)\right)^{-2} \cdot (-1) \cdot (T_{B,Meas.})^{-2} \\ &= T^2 \cdot (T_{B,Meas.})^{-2}\end{aligned} \tag{5.3}$$

- Uncertainty contribution to the true temperature due to the uncertainty of the calculated emissivity:

$$\begin{aligned}\frac{\partial T}{\partial \varepsilon} &= (-1) \cdot \left(\frac{1}{T_B} + \frac{k \cdot \lambda}{c \cdot h} \ln(\varepsilon)\right)^{-2} \cdot \frac{k \cdot \lambda}{c \cdot h} \cdot \frac{1}{\varepsilon} \\ &= (-1) \cdot T^2 \cdot \frac{k \cdot \lambda}{c \cdot h} \cdot \frac{1}{\varepsilon}\end{aligned} \tag{5.4}$$

- The uncertainty of the calculated emissivity is on the other hand determined by the uncertainty of the "black temperature" reading at the solidification plateau $\Delta T_{B,Calibr.}$:

$$\begin{aligned}\frac{\partial \varepsilon}{\partial T_{B,Calibr.}} &= \frac{c \cdot h}{k \cdot \lambda} \cdot \exp\left(\frac{c \cdot h}{k \cdot \lambda}\left(\frac{1}{T} - \frac{1}{T_{B,Calibr.}}\right)\right) \cdot (-1) \cdot (-1) \cdot (T_{B,Calibr.})^{-2} \\ &= \frac{c \cdot h}{k \cdot \lambda} \cdot \varepsilon \cdot (T_{B,Calibr.})^{-2}\end{aligned} \tag{5.5}$$

Using the formulas above, the following sample calculation shall illustrate the contribution of $\Delta T_{B,Meas.}$ and $\Delta T_{B,Calibr.}$ to the uncertainty of the true temperature for a given "black temperature" reading during the measurement. Assuming a "black temperature" reading of $T_{B,Calibr.} = 734\,\mathrm{K}$ at the solidification plateau and a "black temperature" reading of $T_{B,Meas.} = 1000\,\mathrm{K}$ during the measurement, the temperature recalculation with Eq. 3.1 and 3.2 finally yields $T = 1409\,\mathrm{K}$. Taking Eq. 5.2 and applying the terms

from Eq. 5.3, 5.4 and 5.5 results in

$$\begin{aligned}\Delta T &= \sqrt{\left((1409\,\mathrm{K})^2 \cdot (1000\,\mathrm{K})^{-2} \cdot 5\,\mathrm{K}\right)^2} \\ &\quad + \sqrt{\left((-1) \cdot (1409\,\mathrm{K})^2 \cdot (734\,\mathrm{K})^{-2} \cdot 10\,\mathrm{K}\right)^2} \\ &= 38\,\mathrm{K}.\end{aligned}$$

Figure 5.1 shows the effect of the uncertainties of the black temperature readings on the recalculated temperature. Especially at higher temperatures, the recalculated temperature shows a significant difference for two different sets of "black temperature" uncertainties.

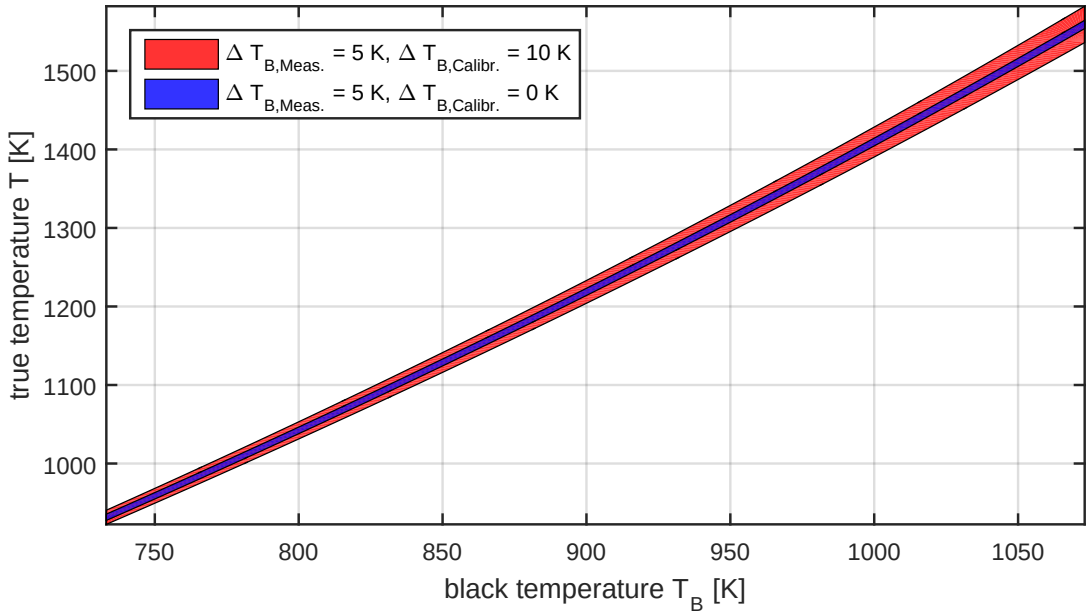

Figure 5.1: Comparison of the influence of $\Delta T_{B,Meas.}$ and $\Delta T_{B,Calibr.}$ on the overall uncertainty of the calculated true temperature. The coloured area illustrates the range in which the true temperature T is located for a given black temperature reading T_B when considering the according uncertainties $\Delta T_{B,Meas.}$ and $\Delta T_{B,Calibr.}$. One can see that the contribution of $\Delta T_{B,Meas.}$ to the overall uncertainty of the true temperature is rather low and does not change significantly with temperature. The contribution of $\Delta T_{B,Calibr.}$ however contributes significantly and non linearly to the overall uncertainty of the true temperature the higher the black temperature reading is.

The described uncertainty of temperature measurement reflects in the specified uncertainty of the values for surface tension and density derived from the according linear fits in Table 6.1. According to the error propagation rules of GUM, the uncertainty of the

calculated values from the linear fits

$$\gamma_l = \gamma_{mp} + \frac{d\gamma}{dT} \cdot (T - T_{mp}) \tag{4.2}$$

$$\rho_l = \rho_{mp} + \frac{d\rho}{dT} \cdot (T - T_{mp}) \tag{4.5}$$

are expressed by

$$\begin{aligned} \Delta\gamma_l &= \sqrt{\left(\frac{\partial\gamma_l}{\partial\gamma_{mp}} \cdot \Delta\gamma_{mp}\right)^2 + \left(\frac{\partial\gamma_l}{\partial\frac{d\gamma}{dT}} \cdot \Delta\frac{d\gamma}{dT}\right)^2 + \left(\frac{\partial\gamma_l}{\partial T} \cdot \Delta T\right)^2} \\ &= \sqrt{(\Delta\gamma_{mp})^2 + \left(T \cdot \Delta\frac{d\gamma}{dT}\right)^2 + \left(\frac{d\gamma}{dT} \cdot \Delta T\right)^2} \end{aligned} \tag{5.6}$$

and

$$\begin{aligned} \Delta\rho_l &= \sqrt{\left(\frac{\partial\rho_l}{\partial\rho_{mp}} \cdot \Delta\rho_{mp}\right)^2 + \left(\frac{\partial\rho_l}{\partial\frac{d\rho}{dT}} \cdot \Delta\frac{d\rho}{dT}\right)^2 + \left(\frac{\partial\rho_l}{\partial T} \cdot \Delta T\right)^2} \\ &= \sqrt{(\Delta\rho_{mp})^2 + \left(T \cdot \Delta\frac{d\rho}{dT}\right)^2 + \left(\frac{d\rho}{dT} \cdot \Delta T\right)^2}. \end{aligned} \tag{5.7}$$

Wien approximation versus Planck's law

Another possible error source that was checked for a non-vanishing contribution to the uncertainty of the true temperature is the method described in Section 3.3 itself. The Equation 3.2 is based on the Wien approximation to describe the spectral radiance as a function of wavelength and temperature [10]

$$L_{\lambda,S}(\lambda, T) = \frac{c_1}{\pi \cdot \Omega_0 \lambda^5} \cdot \frac{1}{\exp\left(\frac{c_2}{\lambda \cdot T}\right)} \tag{5.8}$$

with

$L_{\lambda,S}(\lambda, T)$ ... spectral radiance
λ ... wavelength
T ... temperature
Ω_0 ... solid angle (=1 sr)
c_1 ... 1st radiation constant $\left(= 2 \cdot \pi \cdot c^2 \cdot h\right)$
c_2 ... 2nd radiation constant $\left(= \frac{c \cdot h}{k}\right)$.

When compared to Planck's law

$$L_{\lambda,S}\left(\lambda,T\right)=\frac{c_1}{\pi\cdot\Omega_0\cdot\lambda^5}\cdot\frac{1}{\exp\left(\frac{c_2}{\lambda\cdot T}-1\right)} \tag{5.9}$$

the Wien approximation has the mathematical benefit of the missing term -1 in the denominator after the exponential function. This is advantageous if one tries to transform the relation between the spectral radiance of a "real" body $L_{\lambda,S}(\lambda,T)$ and the spectral radiance of a black body $L_{\lambda,S}(\lambda,T_B(\lambda))$ at the same wavelength and temperature, given by

$$\varepsilon\left(\lambda,T\right)\cdot L_{\lambda,S}\left(\lambda,T\right)=L_{\lambda,S}\left(\lambda,T_B\left(\lambda\right)\right) \tag{5.10}$$

to an explicit expression of form $T=\mathrm{f}(\lambda,T_B)$ where the true temperature can be calculated directly. The quantity $\varepsilon(\lambda,T)$ in Equation 5.10 is called spectral emissivity. An according transformation yields in the Equation 3.2 as presented in section 3.3.

Due to the -1 term in the denominator of Planck's law, equation 5.10 can only be transformed to an equation of the form $T=\mathrm{f}(\lambda,T,T_S)$ where the solution for the temperature T is just given implicitly and thus has to be solved numerically:

$$\frac{1}{\boxed{T}}=\frac{1}{T_S(\lambda)}+\frac{\lambda}{c_2}\cdot\left(\ln\varepsilon\left(\lambda,T\right)+\frac{1-\exp\left(-\frac{c_2}{\lambda\cdot T_S(\lambda)}\right)}{1-\exp\left(-\frac{c_2}{\lambda\cdot\boxed{T}}\right)}\right) \tag{5.11}$$

This is obviously a drawback not only due to higher computational effort but also regarding the uncertainty analysis since a simple explicit expression for the error propagation can not be derived any more.

According to the theory [10], the Wien approximation deviates from the true spectral radiance as described by Planck's law only significantly at high temperatures and large wavelengths (infrared spectrum) when the condition

$$\lambda\cdot T\ll c_2 \tag{5.12}$$

is no longer satisfied. Taking the central wavelength of the bandwidth of the pyrometer used ($\lambda=1.625\,\mu\mathrm{m}$) and assuming a maximum temperature of 1550 K, the product of $\lambda\cdot T$ is approx. $2,5\cdot10^{-3}\,\mathrm{m}\cdot\mathrm{K}$. This is indeed one order of magnitude smaller than $c_2=\frac{c\cdot h}{k}\approx0.0144\,\mathrm{m}\cdot\mathrm{K}$ and the Inequality 5.12 is supposed to be satisfied.

Nevertheless, since the Inequality 5.12 is "only" satisfied by one order of magnitude, the actual difference for the true temperature was calculated for the "worst case" scenario, speaking the highest black temperature reading observed during a measurement. The resulting difference in the true temperature values was only 0.8 K. It was therefore reas-

onable to neglect this inaccuracy and use the Wien approximation for all data evaluation processes.

5.2 Uncertainty budget

In a first step, the uncertainty budgets were created with the software GUM Workbench[2] which applies the rules of error propagation as described by GUM to a given model equation for the quantity of interest, e.g. surface tension or density. For each parameter of the model equation one has to specify whether the input parameter is erroneous (or not) and the according uncertainty of the observable. This is done by either supplying the software with multiple measurement results for the same observable in order to analyse them statistically or by specifying an estimated value for the uncertainty of the observable (further denoted as "Type B" observable). Since there is per measurement point (temperature value) only one value per relevant input parameter (e.g. oscillation frequencies), the latter approach had to be used.

In order to automate the uncertainty analysis, the evaluation scripts in MATLAB were extended. The rules of error propagation were applied to the model equations for surface tension and density and by building the partial derivatives with respect to the different input variables, the overall uncertainty of the quantities could be expressed in explicit functions within MATLAB. The numerical results were then cross checked with the results from GUM Workbench for selected measurement points to verify the correctness of the MATLAB code.

The formulas to calculate the overall uncertainty of each quantity (including all the partial derivatives) are not really necessary for the understanding of the further sections and thus are skipped. Instead, a brief overview of the different contributions to the overall uncertainty of the quantities will be presented in a way similar to the interface of GUM Workbench.

Surface tension

Table 5.1 shows the input parameters for the calculation of the surface tension (see Equation 2.10), their respective configuration in GUM Workbench (e.g. type, distribution, estimated uncertainty) as well as the determined contribution to the overall uncertainty of the calculated surface tension. The standard uncertainty of each translation frequency (ν_x, ν_y, ν_z) was uniformly estimated to a value of 0.1 Hz since they were usually clearly deducible from the according spectra. For each oscillation frequency ($\nu_{2,0}$, $\nu_{2,\pm1}$, $\nu_{2,\pm2}$) however, the standard uncertainty was estimated to be 0.5 Hz since the peaks in the

[2]Version 2.4.1.388, Link: `http://www.metrodata.de/ver24.html`

according spectra were not always clearly visible and assignable as discussed in Section 4.1. The standard uncertainty of the mass of the specimen was estimated to be 0.1 mg, based on the maximum mass loss observed for all specimen ($\Delta m = 0.2\,\mathrm{mg}$).

Table 5.1: Uncertainty budget for the surface tension evaluation created with GUM WORKBENCH.

Type	...	Type of uncertainty for the according quantity A... standard deviation of experimental measurement values B... estimated uncertainty
Distr.	...	probability distribution of the input quantity N... Normal, R... Rectangular
Sensitivity Coefficient	...	expression how the surface tension γ_l varies with changes in the according input quantity x (corresponds to partial derivate $\frac{\partial \gamma_l}{\partial x}$)
Uncertainty Contribution	...	corresponds to the product of the sensitivity coefficient and the standard uncertainty of the according quantity
Index	...	percentage of the variance stemming from the according input quantity

Qty	**Type, Distr.**	**Value**	**Standard Uncertainty**	**Sensitivity Coefficient**	**Uncertainty Contribution**	**Index**
m	B, N	110.8 mg	0.1 mg	+7.3	$+0.73\,\mathrm{mN \cdot m^{-1}}$	2.3 %
ρ	B, N	$2307\,\mathrm{kg \cdot m^{-3}}$	$8\,\mathrm{kg \cdot m^{-3}}$	$-680 \cdot 10^{-6}$	$-5.4 \cdot 10^{-3}\,\mathrm{mN \cdot m^{-1}}$	0.0 %
ν_x	B, N	10.50 Hz	0.1 Hz	−1.7	$-0.17\,\mathrm{mN \cdot m^{-1}}$	0.1 %
ν_y	B, N	9.28 Hz	0.1 Hz	−1.5	$-0.15\,\mathrm{mN \cdot m^{-1}}$	0.0 %
ν_z	B, N	20.26 Hz	0.1 Hz	−3.2	$-0.32\,\mathrm{mN \cdot m^{-1}}$	0.4 %
$\nu_{2,0}$	B, N	83.74 Hz	0.5 Hz	+4.4	$+2.2\,\mathrm{mN \cdot m^{-1}}$	20.6 %
$\nu_{2,-1}$	B, N	78.86 Hz	0.5 Hz	+4.4	$+2.2\,\mathrm{mN \cdot m^{-1}}$	20.8 %
$\nu_{2,+1}$	B, N	89.60 Hz	0.5 Hz	+4.4	$+2.2\,\mathrm{mN \cdot m^{-1}}$	20.8 %
$\nu_{2,-2}$	B, N	67.38 Hz	0.5 Hz	+4.0	$+2.0\,\mathrm{mN \cdot m^{-1}}$	17.4 %
$\nu_{2,+2}$	B, N	86.91 Hz	0.5 Hz	+4.0	$+2.0\,\mathrm{mN \cdot m^{-1}}$	17.4 %

One can see from Table 5.1 that only the oscillation frequencies and the mass give a significant contribution to the uncertainty of the calculated surface tension. The uncertainties of the translation frequencies have almost no effect on the overall uncertainty.

Density

In case of the density evaluation, the uncertainty analysis appears very simple at first sight but is indeed quite complicated. Due to the very simple model equation for the density ($\rho = \frac{m}{V}$), applying the rules of error propagation results in a very simple formula for the uncertainty of the calculated density:

$$\Delta\rho = \sqrt{\left(\frac{d\rho}{dm} \cdot \Delta m\right)^2 + \left(\frac{d\rho}{dV} \cdot \Delta V\right)^2}$$

So only the uncertainty of the two input parameters mass and volume has to be considered. The standard uncertainty of the mass was again estimated to be 0.1 mg. But the problem here is to estimate the standard uncertainty of the volume, which is not a direct observable. Due to the sophisticated method described in Section 3.5 that is used to determine the actual volume of the specimen, it is almost impossible to quantify possible inaccuracies of the numerous intermediate steps performed with the different programs. The possible error sources are (hierarchically):

- Edge detection process
- Fitting of radii - data with Legendre polynomial
- Calculating the specimen volume under the assumption of a vertical axis symmetry.

The possibly biggest error may stem from the assumption of vertical axis symmetry. Although the averaging over a long time (typically 4100 images) performed in the evaluation process should compensate for those effects, the specimen may still show a permanent deformation from vertical axis symmetry due to the "magnetic pressure" applied by the levitation coils. Especially the latter effect but also the other possible error sources listed above have to be classified as systematic errors for which the numerical value can possibly be estimated by comparison with the literature values.

The standard uncertainty of the calculated density values due to a random error during the measurement may be estimated from the scatter of the data points, as described in [4], where the uncertainty of density was estimated to be about 2 %. Nevertheless, this value should be adapted in the case of aluminium as sample material since the scatter in Figure 4.8 shows a larger value.

5.3 Other influences possibly contributing to the uncertainty

Frequency generator

During this thesis, the question arose at which frequency the alternating current is oscillating inside the levitation coils and how large the current actually is. For this purpose, a so called Rogowski coil was used[3].

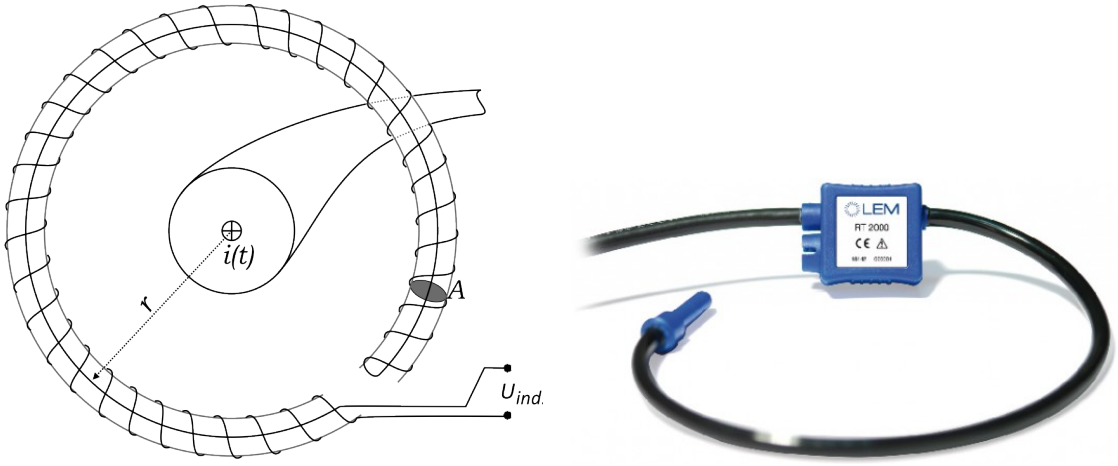

Figure 5.2: Left: Schematic illustration of a Rogowski coil (Source: Adapted from [36]). Right: Picture of the LEM RT 2000 Rogowski coil (Source of image: [37]).

A Rogowski coil is a helical coil of wire, which is wounded around the non-conducting, non-ferromagnetic core of the coil. This is why the Rogowski coil is also called "air-coil". The Rogowski coil allows a non-contact measurement of alternating currents or current pulses based on the principle of electromagnetic induction. The voltage induced $U_{ind.}$ by the current I is proportional to the rate of change of the current to measure:

$$U_{ind.} \propto \frac{dI}{dt} \tag{5.13}$$

As a consequence, the induced voltage is also time dependent and shows for periodic signals (e.g. sinusoidal) a phase shift to the current to measure of $\Delta\varphi = \pi/2$.

The Rogowski coil was mounted for practical reasons outside the probe chamber around one power supply tube of the electric circuit near the feedthrough to the probe chamber. In addition, the voltage between the two power supply tubes U_{AC} was measured at the same position. The measurement performed qualitatively with an oscilloscope[4] showed a frequency of the alternating current of about $f = 380\,\text{kHz}$ and current values up to $I_{rms} = 350\,\text{A}$, whereas the voltage was about $U_{rms} = 400\,\text{V}$. Depending on the polarity

[3] LEM RT 2000
[4] Rigol DS1052E, for more details see the equipment list on page 64

of the measurement wires, the phase shift between the signal of the Rogowski $U_{ind.}$ coil and the voltage U_{AC} was either almost $\Delta\varphi = \pi$ or $\Delta\varphi = 0$. Remembering that there is already a systematic phase shift of $\Delta\varphi = \pi/2$ due to the measurement principle of the Rogowski coil (see Equation 5.13) this shows that there is obviously a real phase shift between the alternating current I_{AC} and the alternating voltage U_{AC} of almost $\Delta\varphi = \pi/2$. This shows that there is only little active power but large reactive power.

An unexpected observation during those measurements was that neither the measured current nor the measured voltage changed when the output power of the frequency generator was varied. But by enlarging the time period on the oscilloscope, another periodic signal with approx. 144 Hz showed up which explains the latter phenomenon. The power control of the frequency generator obviously just controls the duty cycle of the output current at fixed output voltage, not the current and voltage itself, whereas the power pulse is clocked with approx. 144 Hz as illustrated in Figure 5.3.

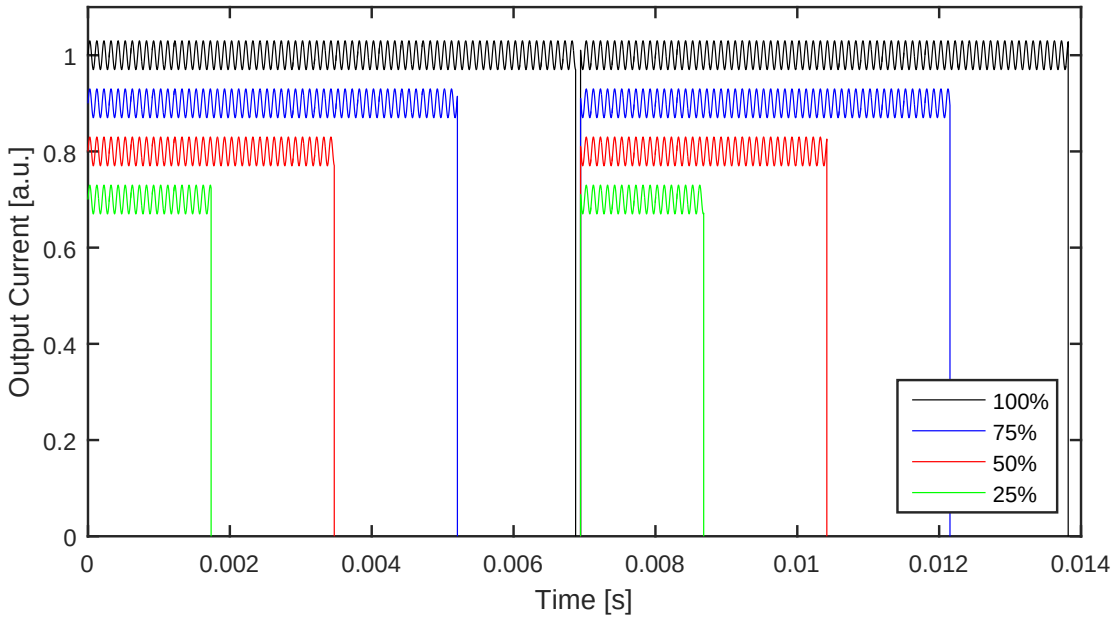

Figure 5.3: Illustration depicting the duty cycle of the high frequency generator. The power regulator just controls the duration of the output pulses, not the amplitude of the voltage or current. The duration between two consecutive pulses is approx. 7 ms which corresponds to a frequency of approx. 144 Hz. At maximum power, the gap between two pulses almost vanishes, else the length of the pulse is adjusted according to the selected output power level. The output current during a pulse oscillates with approx. 380 kHz but is illustrated in this figure with a frequency of 10 kHz for better visibility. For the same reason each of the lines is impinged with an offset with respect to the baseline of the coordinate system in order to separate the different lines.

It is now questionable if the clocking of the high frequency generator and thus the

clocking of the electromagnetic field is inducing oscillations with this frequency or possibly enforcing oscillations with frequencies near fractions of the cycling frequency (e.g. $f/2 = 72\,\mathrm{Hz}$). This is a possible explanation why the peaks of related oscillation modes (modes with same values of m, especially the modes $\nu_{2,\pm 2}$, see Section 3.5), do show a significant difference in height.

6 Summary

The scope here is to briefly summarize the key findings which are concluded in Section 6.1. In addition, an outlook is given in Section 6.2, where some considerations to improve the experimental setup as well as the data evaluation are discussed.

6.1 Conclusion

Two thermophysical properties of aluminium, surface tension and density, were investigated by performing experiments with the electromagnetic levitation method. This thesis was motivated by the need to benchmark the recently installed electromagnetic levitation setup by measuring pure metals where data from literature were already available for comparison.

Aluminium as sample material was chosen since it was expected to bring up experimental challenges due to its characteristics (melting temperature, affinity to oxygen, electrical conductivity) being very different to every other sample material investigated before. Special attention was paid to those challenging characteristics and their consequences for the measurement procedure (as described in detail in Section 4.1), whereas the consequences for the quality of the measured data itself was discussed in Sections 5.1 and 5.2. In the latter section, other possible effects influencing the data accuracy as well as an uncertainty budget for both, surface tension and density, was presented. A short list of the findings of the sections listed above:

- As a result of the low melting temperature of aluminium, it was not possible to take thermal radiation images of the specimens at temperatures near the melting temperature. Thus, no surface tension data could be obtained in this temperature range, although it is of special interest for metalworking industry. It was however achieved to tune the experimental setup and the image acquisition process during this thesis to obtain data as close as $(1014 \pm 21)\,\mathrm{K}$ to the melting temperature.
- The affinity of aluminium to build aluminium oxide instantaneously in the presence of oxygen in the atmosphere affected the measurement in different ways. The influence of the oxide islands on the temperature measurement was severe, especially at temperatures below $1100\,\mathrm{K}$, due to their different spectral emissivity

compared to the clean aluminium surface. The surface tension data obtained by the measurements had thus to be categorized as oxygen - contaminated. Moreover, a repetition of a measurement run with the same sample was impossible since the aluminium oxide layer built at low temperatures was very rigid and prevented another phase transition to the liquid state. Nevertheless, the measurement procedure was optimized as the thesis progressed in order to minimize these effects as much as possible.

- Aluminium's high electrical conductivity was advantageous concerning the stability of the levitation process, the drawback however was the low heating of the specimen (when compared to other materials). As a consequence, it was not possible to overcome an upper temperature limit of 1550 K, although it would have been favourable to overcome this limit in order to improve the stability of the linear fit obtained for the measurement data. Moreover, the low heating of aluminium was certainly another reason why the specimens covered by the oxide layer could not be melted any more.

The measurement results obtained for the surface tension show a good agreement with many data from the public literature (see Section 4.2). The slight shift of the data to larger surface tension values is assumed to stem from comparably clean specimens regarding the aluminium oxide content since surface tension data of (claimed) oxygen-free aluminium in the literature are significantly larger than all other literature data, which therefore have to be assumed oxygen-contaminated too. A linear model equation was applied to the data points

$$\gamma_l = \gamma_{mp} + \frac{d\gamma}{dT} \cdot (T - T_{mp}) \tag{4.2}$$

and the following fit parameters were obtained

$$\gamma_{mp} = (880 \pm 2)\,\mathrm{mN} \cdot \mathrm{m}^{-1} \tag{4.3}$$

$$\frac{d\gamma}{dT} = -(0.128 \pm 0.004)\,\mathrm{mN} \cdot \mathrm{m}^{-1} \cdot \mathrm{K}^{-1}. \tag{4.4}$$

When comparing the density measurements with data available in public literature, it shows overall a satisfying agreement (see Section 4.2) but there is still a shift of the measurement data to lower density values that can not be neglected. Nevertheless, data from a quite recent publication (where the data was obtained by electromagnetic levitation too) appears to coincide with the measurement results of this thesis. Unfortunately, a comparison of the results of this publication with literature data already available is missing and therefore the discussion about the possible reasons for this offset too. The offset is therefore assumed to be most probably the result of a slight systematic over-

estimation of the actual specimen volume, a phenomenon that can not be dismissed with certainty. Again, a linear model equation was applied to the data

$$\rho_l = \rho_{mp} + \frac{d\rho}{dT} \cdot (T - T_{mp}) \tag{4.5}$$

and the following fit parameters were obtained

$$\rho_{mp} = (2307 \pm 8)\,\mathrm{kg \cdot m^{-3}} \tag{4.6}$$

$$\frac{d\rho}{dT} = -(0.29 \pm 0.03)\,\mathrm{kg \cdot m^{-3} \cdot K^{-1}}. \tag{4.7}$$

For convenience, a lookup table (see appendix at page 63) with numerical values for surface tension and density at different temperatures (steps of 20 K) was calculated from the model equations with the according fit parameters.

6.2 Outlook

With the ongoing progress of this thesis, several ideas were formulated within the work group how the experimental setup as well as the evaluation process could be improved in order to minimize or bypass certain problems described in the chapters before.

Alternative evaluation of the thermal radiation images

For the present surface tension evaluation, an edge detection algorithm was applied to the thermal radiation images in order to get the radii from the centre of mass to the edge of the specimen in 5 ° steps (as described in Section 3.5). In a next step, the time evolution of two perpendicular radii was analysed in order to generate a spectrum by a Fast Fourier Transform. This evaluation method is however vulnerable to inaccuracies of the edge detection process, since the sum and difference of the perpendicular radii is strongly affected if the inaccuracies distort one radius more than the other one. This type of inaccuracy may appear in case of bad contrast thermal radiation images at low temperatures or blurry edges due to long shutter times.

The proposed change in the evaluation method now is to use two perpendicular areas instead of two perpendicular radii. Each area is to be calculated between a set of two secants centred around the centre of mass, whereby the two sets of secants are perpendicular to each other, as it is illustrated in Figure 6.1.

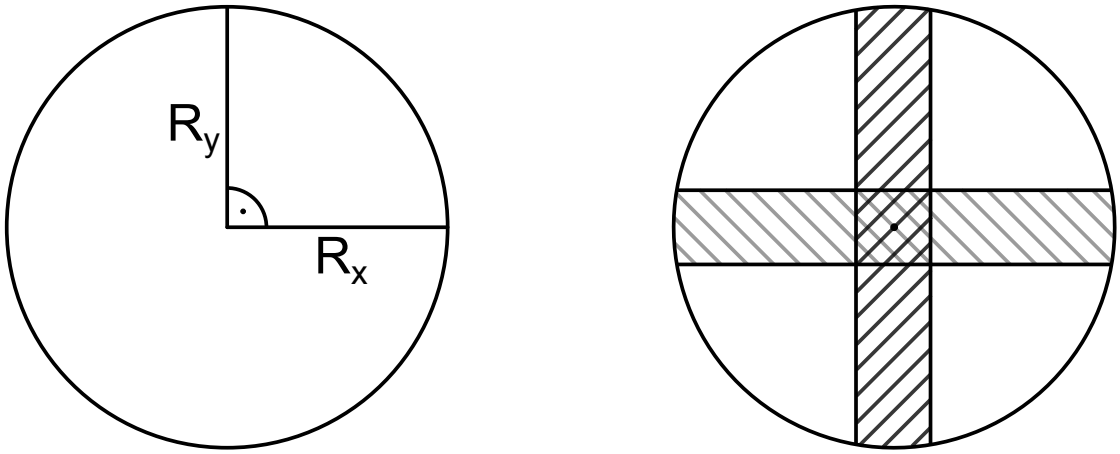

Figure 6.1: Left: Present evaluation method for the thermal radiation images based on two perpendicular radii. Right: Illustration of the suggested new thermal radiation image evaluation based on two perpendicular areas.

Additionally, the distance between each secant set may be variable in order to gain another parameter to tune during evaluation in case of sophisticated spectra. By using this approach, particularly the spectra of bad contrast images or images with blurry edges should have a better signal to noise ratio since this method introduces a certain averaging effect. But even the evaluation of "nice" thermal radiation images with good contrast and sharp edges may benefit from this approach.

Background illumination from bottom

The more definite approach would be to install a background illumination system placed below the specimen in order to be able to record shadowgraphs for the surface tension evaluation. Since only the correct detection of the deformation of the specimen rather than the actual size is important for the surface tension evaluation, even an inhomogeneous background illumination would probably do a good job in case of sample materials with low melting temperatures (like aluminium).

This solution however requires several modifications on the experimental setup since the linear feedthrough, on which the sample holder is mounted, is positioned below the specimen. Thus, the bottom of the probe chamber can not be replaced by a window and the background illumination can only be installed inside the probe chamber. This again would require an additional feedthrough or a similar solution in order to supply the background illumination with electricity. Moreover, the light source inside the probe chamber has to withstand the evacuation process which most likely limits the number of available devices.

Another possibility to evaluate is to install a mirror inside the probe chamber so that

the light source can still be placed outside the probe chamber. But there is still the (geometric) problem to solve how to arrange both, mirror and sample holder, in a satisfying way.

Oxygen detection system

For a better reproducibility of the measurements, the expansion of the measurement setup with an oxygen detection system would be advantageous and is already planned to be realized as part of a future research project. Not only in case of aluminium the knowledge of the oxygen partial pressure would be of great interest since it adds an additional experimental observable which allows a more sophisticated comparison of the measurement results due to the great influence of impurities (e.g. oxides) on the surface tension. Kobatake et al. [19] installed a similar system and obtained measurement results for aluminium in an oxygen-reduced environment. Another group in a related field (Schulz et al. [38]) even made a step further and already realised a control system for the oxygen partial pressure for microgravity experiments executed at the levitation facility onboard the international space station ISS. The installation of an according control system is therefore also a feature of interest for future extension of the experimental setup.

Measurement of spectral emissivity

The "ultimate" solution to the problem of oxides on the specimen's surface compromising the temperature measurement via pyrometer is a real-time measurement of the spectral emissivity of the specimen's surface during the experiment. Using this approach, even the calibration of the pyrometer at the melting or solidification plateau could be omitted since the spectral emissivity is measured continuously.

A device to measure the normal spectral emissivity is a Division of Amplitude Polarimeter (DOAP). The thermophysics and metalphysics group at TU Graz already has a µs-DOAP device with microsecond resolution which was used in the past together with the microsecond pulse-heating setup to determine the normal spectral emissivity of wire-shaped specimen. Figure 6.2 shows the working principle of the µs-DOAP used in the pulse-heating setup. Nevertheless, it is not usable in it's current configuration as it measures the normal spectral emissivity at a wavelength different to the wavelength of the pyrometer (DOAP: 684.5 nm, Pyrometer: 1625 nm).

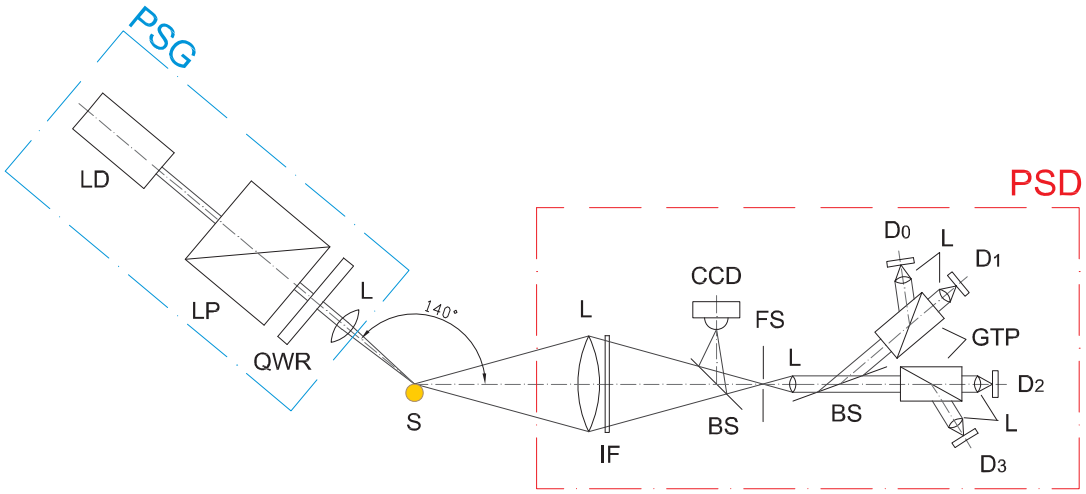

Figure 6.2: Schematic illustration of the µs-DOAP as it was used in the pulse heating setup. It consists of the polarisation state generator (PSG) and the polarisation state detector (PSD), drawing an angle of 140 °. The yellow dot in the middle illustrates the specimen. The single components are:
PSG: LD . . . diode laser, LP. . . linear polarizer, QWR . . . quarter wave retarder, L . . . lens;
PSD: L . . . Lens, IF . . . interference filter, BS . . . beam splitter, CCD . . . camera, FS . . . field stop, GTP . . . Glan-Thompsonprism, D0-D3. . . detectors. Figure taken from [39].

Since an angle between the polarization state generator (PSG) and the polarisation state detector (PSD) of 140 ° has to be ensured, the present experimental setup with opposite windows has to be evaluated whether it allows the arrangement of PSG and PSD in a way that this requirement can be satisfied without compromising the other components of the setup (pyrometer, background illumination for density measurements, etc.) or not. Otherwise, the probe chamber has to be extended by two additional windows. Nevertheless, the present windows are not suitable for usage of a DOAP, since the window material must not change the polarisation of the transmitted light. Thus windows of a different material have to be used, e.g. BK7 glass (Borosilicate glass).

Synchronised cameras

At the start of this thesis, a quick switching between the two cameras (top and side view of the specimen) was not possible. While this drawback was fixed during the work on this thesis by extending the image capture software, the idea to take a further step was not yet implemented. This next step would be the time synchronised acquisition of images from the top and side view, which would allow to decide within the density evaluation if the assumption of vertical axis symmetry was correct or not. This would allow to

exclude image sequences from the density evaluation where the assumption from the ideal spherical shape and vertical axis symmetry was violated by large distortions. Not only the accuracy of the obtained density results in general could be improved but also the problem of the systematic over-estimation of the specimen's volume could possibly be solved by using this approach.

One problem in the realization is certainly the difference in frame rate between the two cameras used, since the density camera is limited to 120 fps, whereas the surface tension camera is usually configured to operate at significantly higher frame rates typically greater than 600 fps. Fortunately, the frame rate of the surface tension camera can be reduced quite easily via software interface as this was already shown in Section 4.1. The main challenge is probably the adaption of the image acquisition software and the addressing of the software library that controls the image grabber card in order to lower the frame rate of the surface tension camera to the frame rate value of the density camera.

It might be worth considering the acquisition of an additional high-speed camera with a frame rate greater than 500 fps (e.g. 2^{nd} device of the present surface tension camera) in order to benefit from the time-synchronized images within the surface tension evaluation as well. This may help to reconstruct the specimen's oscillations by analysing both, the spectra of the top and side view.

Appendix

Table 6.1: Values for surface tension and density calculated from the fit equations and parameters in Section 4.2.

T ... Temperature
γ ... Surface tension
ρ ... Density

T [K]	γ [mN·m^{-1}]	ρ [kg·m^{-3}]	T [K]	γ [mN·m^{-1}]	ρ [kg·m^{-3}]
933[1]	880 ± 2	2307 ± 15	1280	836 ± 3	2206 ± 20
940	879 ± 2	2305 ± 15	1300	833 ± 3	2201 ± 20
960	877 ± 2	2299 ± 15	1320	830 ± 4	2195 ± 21
980	874 ± 3	2293 ± 15	1340	828 ± 4	2189 ± 21
1000	871 ± 3	2288 ± 16	1360	825 ± 4	2183 ± 21
1020	869 ± 3	2282 ± 16	1380	823 ± 4	2177 ± 22
1040	866 ± 3	2276 ± 16	1400	820 ± 4	2172 ± 22
1060	864 ± 3	2270 ± 17	1420	818 ± 4	2166 ± 22
1080	861 ± 3	2264 ± 17	1440	815 ± 4	2160 ± 23
1100	859 ± 3	2259 ± 17	1460	813 ± 4	2154 ± 23
1120	856 ± 3	2253 ± 18	1480	810 ± 4	2148 ± 23
1140	854 ± 3	2247 ± 18	1500	807 ± 4	2143 ± 24
1160	851 ± 3	2241 ± 18	1520	805 ± 4	2137 ± 24
1180	848 ± 3	2235 ± 19	1540	802 ± 4	2131 ± 24
1200	846 ± 3	2230 ± 19	1560	800 ± 4	2125 ± 25
1220	843 ± 3	2224 ± 19	1580	797 ± 4	2119 ± 25
1240	841 ± 3	2218 ± 20	1600	795 ± 5	2114 ± 25
1260	838 ± 3	2212 ± 20			

[1] Melting point of aluminium

Equipment list

Power supply:

- High frequency generator:
  - IG 5/200HY, Trumpf Hüttinger GmbH + Co. KG
  - Important figures: $f \approx 380\,\mathrm{kHz}$, $I_{rms} \approx 350\,\mathrm{A}$, duty cycle of $f \approx 144\,\mathrm{Hz}$
- Cooling device:
  - Kühlmobil 141, Van der Heijden - Labortechnik GmbH

Vacuum system

- Rotary Vane Pump:
  - Pfeiffer Balzers Duo 0016B, Pfeiffer Vacuum GmbH
    - For pressures down to $10^{-2}\,\mathrm{mbar}$
- Turbomolecular pump:
  - Pfeiffer Balzers TPU 330, Pfeiffer Vacuum GmbH
    - For pressures down to $10^{-6}\,\mathrm{mbar}$
- Pressure gauges:
  - pressure range: $< 10^{-3}\,\mathrm{mbar}$:
    - Pfeiffer Balzers IKR-020, Pfeiffer Vacuum GmbH
      - Type: Cold cathode gauge
  - pressure range: $(10^{-4} - 1)\,\mathrm{mbar}$
    - TPR-016, Pfeiffer Vacuum GmbH
      - Type: Pirani gauge
  - pressure range: $(1 - 2000)\,\mathrm{mbar}$
    - Leybold DI 2000, Oerlikon Leybold Vacuum GmbH
      - Measurement principle: deforming membrane as part of capacitance measurement circuit

Gas supply:

- Gas (mixtures):
  - Alphagaz 1 Argon (purity: $\geq 99.999\,\%\,\mathrm{mol}$), Air Liquide
  - Alphagaz 2 Helium (purity: $\geq 99.9999\,\%\,\mathrm{mol}$), Air Liquide
  - Arcal 10 (97.6 vol% Ar, 2.4 vol% H_2) , Air Liquide
  - custom mixture of He + 4% H2, Air Liquide
- Oxygen purification system:
  - Oxisorb©, Messer Group GmbH
    - $O_2 < 5\,\mathrm{ppb}$, H_2O: $< 30\,\mathrm{ppb}$

Imaging System:

- Framegrabber:
  - Matrox Radient eCL, Matrox Imaging
- high speed camera (surface tension):
  - Mikrotron EoSens® CL, Mikrotron GmbH
    - Detector: CMOS
    - Max. framerate of 506 fps at full resolution (1280 px x 1024 px)
- 2nd high speed camera (density):
  - Basler avA1000 - 120km, Basler AG
    - Detector: CCD
    - Max. framerate of 120 fps; Resolution: 1024 px x 1024 px
- Lens:
  - 2x AF Micro-Nikkor ED 200 mm f/4 D IF, Nikon Corporation

Temperature measurement (Pyrometer):

- IMPAC IGA 6 Advanced, LumaSense Technologies
  - Spectral range: $(1.45 - 1.8)\,\mu\mathrm{m}$
  - Temperature range: $\approx (250 - 2500)\,°\mathrm{C}$
  - Response time: $120\,\mu\mathrm{s}$

Various:

- Ultrasonic Bath:
  - Emag Technologies® Emmi® - 20HC
    - Cleaning frequency: 45 kHz; Temperature: $(20 - 80)$ °C
- Precision balance:
  - Mettler Toledo AB104-S-A
    - Readability: 0.1 mg, Repeatability: 0.1 mg, Max. capacity: 101 g
- Oscilloscope
  - Rigol DS1052E
    - 2 channels; Bandwidth 50 MHz; Sample rate max. 1 GSa/s

ADVENT
Advent Research Materials Ltd
Oakfield Industrial Estate
Eynsham · Oxford
England OX29 4JA
Tel + 44 1865 884440
Fax+ 44 1865 884460
info@advent-rm.com
www.advent-rm.com

23rd July 2012

Certificate of Analysis

Aluminium High Purity 99.999%
Catalogue Nos Al 501907 to Al 501912 & Al 501900
Diameter 5.0mm
Batch No. Gi376

LABORATORY REPORT

Typical analysis ppm: Ag 0.121, As 0.159, Au<0.01, K 0.043, B 0.047, La 0.046, Ba 0.076, Li 0.006, Be 0.008, Mg 1.325, Bi 0.040, Mn 0.056, C<1.0, Mo 0.050, Ca 0.110, N <1.0, Ce 0.124, Na 0.237, Cl 0.158, Ni 0.036, Co 0.009, O <1.0, Cr 0.038, P 1.287, Cs 0.024, Pb 0.031, Cu 0.308, Pd 0.035, F 0.032, Pt 0.223, Fe 0.365, S 0.091, Ga 0.225, Sb 0.049, Ge 0.148, Si 1.228, In 0.034, Sn 0.137, Ti 0.104, Th 0.071, U 0.019, V 0.014, Zn 0.098, Zr 0.074, H <0.2. Balance Al.

ADVENT Research Materials Ltd
Quality Assurance

Bibliography

[1] S. Neves, W. Schäfer, and P. N. Hansen. The sensibility of thermophysical property data for simulating casting processes. *International Journal of Thermophysics*, 23(5):1391–1399, 2002. doi:10.1023/A:1019877211862.

[2] T. E. of Encyclopædia Britannica. Aluminium (al) — encyclopædia britannica online, 2016. [Online; accessed 02-September-2016]. URL: https://www.britannica.com/science/aluminum.

[3] K. Aziz. *Surface Tension Measurements of Liquid Metals and Alloys by Oscillating Drop Technique in combination with an Electromagnetic Levitation Device.* PhD thesis, Graz University of Technology, 2016. URL: https://www.tugraz.at/fileadmin/user_upload/Institute/IEP/Thermophysics_Group/Files/Diss-AzizKirmanj.pdf.

[4] A. Schmon. *Density Determination of Liquid Metals by Means of Containerless Techniques.* PhD thesis, Graz University of Technology, 2016. URL: https://www.tugraz.at/fileadmin/user_upload/Institute/IEP/Thermophysics_Group/Files/Diss-SchmonAlexander.pdf.

[5] I. Egry, G. Lohöfer, and S. Sauerland. Measurements of thermophysical properties of liquid metals by noncontact techniques. *International Journal of Thermophysics*, 14(3):573–584, may 1993. doi:10.1007/BF00566054.

[6] I. Egry, E. Ricci, R. Novakovic, and S. Ozawa. Surface tension of liquid metals and alloys - recent developments. *Advances in Colloid and Interface Science*, 159(2):198–212, sep 2010. doi:http://dx.doi.org/10.1016/j.cis.2010.06.009.

[7] J. Lee, D. M. Matson, S. Binder, M. Kolbe, D. Herlach, and R. W. Hyers. Magnetohydrodynamic modeling and experimental validation of convection inside electromagnetically levitated co-cu droplets. *Metallurgical and Materials Transactions B*, 45(3):1018–1023, dec 2014. doi:10.1007/s11663-013-9995-5.

[8] D. L. Cummings and D. A. Blackburn. Oscillations of magnetically levitated aspherical droplets. *Journal of Fluid Mechanics*, 224:395–416, mar 1991. doi:10.1017/S0022112091001817.

[9] I. Egry, H. Giffard, and S. Schneider. The oscillating drop technique revisited. *Measurement Science and Technology*, 16(2):426, jan 2005. doi:http://dx.doi.org/10.1088/0957-0233/16/2/013.

[10] F. Henning. *Temperaturmessung*. Springer Science + Business Media, 1977. doi:10.1007/978-3-642-81138-8.

[11] D. R. Lide. *CRC Handbook of Chemistry and Physics, 84th Edition*. Taylor & Francis, 2003. URL: https://www.crcpress.com/CRC-Handbook-of-Chemistry-and-Physics-84th-Edition/Lide/p/book/9780849304842.

[12] K. Aziz, A. Schmon, E. Kaschnitz, J. Rattenberger, and G. Pottlacher. Measurement of surface tension of cu-5sn by an oscillating drop - levitation technique. *International Journal of Thermophysics*, 37(2):15, jan 2016. doi:10.1007/s10765-015-2023-z.

[13] T. Campbell, R. K. Kalia, A. Nakano, P. Vashishta, S. Ogata, and S. Rodgers. Dynamics of oxidation of aluminum nanoclusters using variable charge molecular-dynamics simulations on parallel computers. *Phys. Rev. Lett.*, 82(24):4866–4869, jun 1999. doi:10.1103/PhysRevLett.82.4866.

[14] O. Braaten, A. Kjekshus, and H. Kvande. The possible reduction of alumina to aluminum using hydrogen. *JOM*, 52(2):47–53, feb 2000. doi:10.1007/s11837-000-0047-7.

[15] C. E. Shannon. Communication in the presence of noise. *Proc. Institute of Radio Engineers*, 37(1):10–21, Jan. 1949.

[16] K. Aziz, A. Schmon, and G. Pottlacher. Measurement of surface tension of liquid nickel by the oscillating drop technique. *High Temperatures – High Pressures*, 44(6):475–481, 2015.

[17] General physical properties. In W. Gale and T. Totemeier, editors, *Smithells Metals Reference Book (Eighth Edition)*, pages 14–1–14–45. Elsevier BV, Oxford, eighth edition edition, 2004. URL: http://dx.doi.org/10.1016/B978-075067509-3/50017-8, doi:10.1016/b978-075067509-3/50017-8.

[18] J. Brillo and G. Kolland. Surface tension of liquid al–au binary alloys. *Journal of Materials Science*, 51(10):4888–4901, feb 2016. doi:10.1007/s10853-016-9794-x.

[19] H. Kobatake, J. Brillo, J. Schmitz, and P.-Y. Pichon. Surface tension of binary al–si liquid alloys. *Journal of Materials Science*, 50(9):3351–3360, 2015. doi:10.1007/s10853-015-8883-6.

[20] J. Molina, R. Voytovych, E. Louis, and N. Eustathopoulos. The surface tension of liquid aluminium in high vacuum: The role of surface condition. *In-*

ternational journal of adhesion and adhesives, 27(5):394–401, jul 2007. doi:10.1016/j.ijadhadh.2006.09.006.

[21] K. C. Mills. Al pure aluminium. In K. C. Mills, editor, *Recommended Values of Thermophysical Properties for Selected Commercial Alloys*, Woodhead Publishing Series in Metals and Surface Engineering, pages 19–25. Woodhead Publishing, 2002. doi:http://dx.doi.org/10.1533/9781845690144.19.

[22] N. Eustathopoulus. Chapter 4 surface energies. In M. G. N. Nicolas Eustathopoulus and B. Drevet, editors, *Wettability at High Temperatures*, volume 3 of *Pergamon Materials Series*, pages 148–174. Pergamon, 1999. doi:http://dx.doi.org/10.1016/S1470-1804(99)80006-6.

[23] A. Pamies, C. G. Cordovilla, and E. Louis. The measurement of surface tension of liquid aluminium by means of the maximum bubble pressure method: the effect of surface oxidation. *Scripta metallurgica*, 18(9):869–872, 1984.

[24] L. Goumiri, J. Joud, P. Desre, and J. Hicter. Tensions superficielles d'alliages liquides binaires présentant un caractère dimmiscibilité: Al-pb, al-bi, al-sn et zn-bi. *Surface Science*, 83(2):471–486, may 1979. doi:http://dx.doi.org/10.1016/0039-6028(79)90057-8.

[25] P. Laty, J. Joud, P. Desré, and G. Lang. Tension superficielle d'alliages liquides aluminium-cuivre. *Surface Science*, 69(2):508–520, 1977. doi:http://dx.doi.org/10.1016/0039-6028(77)90130-3.

[26] B. J. Keene. Review of data for the surface tension of pure metals. *International Materials Reviews*, 38(4):157–192, jan 1993. doi:10.1179/imr.1993.38.4.157.

[27] J. Schmitz, B. Hallstedt, J. Brillo, I. Egry, and M. Schick. Density and thermal expansion of liquid al–si alloys. *Journal of Materials Science*, 47(8):3706–3712, jan 2012. doi:10.1007/s10853-011-6219-8.

[28] J. Brillo, I. Egry, and J. Westphal. Density and thermal expansion of liquid binary al–ag and al–cu alloys. *International Journal of Materials Research*, 99(2):162–167, 2008.

[29] H. L. Peng, T. Voigtmann, G. Kolland, H. Kobatake, and J. Brillo. Structural and dynamical properties of liquid al-au alloys. *Phys. Rev. B*, 92(18):184201, Nov 2015. doi:10.1103/PhysRevB.92.184201.

[30] T. Iida and R. Guthrie. *The Thermophysical Properties of Metallic Liquids: Predictive Models*. The Thermophysical Properties of Metallic Liquids. Oxford University Press, oct 2015. doi:10.1093/acprof:oso/9780198729846.001.0001.

[31] M. J. Assael, K. Kakosimos, R. M. Banish, J. Brillo, I. Egry, R. Brooks, P. N. Quested, K. C. Mills, A. Nagashima, Y. Sato, and W. A. Wakeham. Reference data

for the density and viscosity of liquid aluminum and liquid iron. *Journal of Physical and Chemical Reference Data*, 35(1):285–300, 2006. doi:10.1063/1.2149380.

[32] P. M. Smith, J. W. Elmer, and G. F. Gallegos. Measurement of the density of liquid aluminum alloys by an x-ray attenuation technique. *Scripta Materialia*, 40(8):937–941, mar 1999. doi:10.1016/S1359-6462(99)00043-3.

[33] P. M. Nasch and S. G. Steinemann. Density and thermal expansion of molten manganese, iron, nickel, copper, aluminum and tin by means of the gamma-ray attenuation technique. *Physics and Chemistry of Liquids*, 29(1):43–58, jan 1995. doi:10.1080/00319109508030263.

[34] I. Egry, J. Brillo, D. Holland-Moritz, and Y. Plevachuk. The surface tension of liquid aluminium-based alloys. *Materials Science and Engineering: A*, 495(1–2):14–18, nov 2008. Fifth International Conference on High Temperature Capillarity HTC-2007, Alicante, Spain. doi:http://dx.doi.org/10.1016/j.msea.2007.07.104.

[35] BIPM. Evaluation of measurement data - guide to the expression of uncertainty in measurement, 2008.

[36] Wikipedia. Rogowski coil — wikipedia, the free encyclopedia, 2016. [Online; accessed 28-August-2016]. URL: https://en.wikipedia.org/w/index.php?title=Rogowski_coil&oldid=716824701.

[37] L. I. S. Website. Lem's new class of rogowski coil split-core current transducers: The rt series, 2016. [Online; accessed 27-August-2016]. URL: http://lemcity.com/lems-new-class-of-rogowski-coil-split-core-current-transducers-the-rt-series/.

[38] M. Schulz, J. Brillo, C. Stenzel, and H. Fritze. Oxygen partial pressure control for microgravity experiments. *Solid State Ionics*, 225:332–336, oct 2012. Solid State Ionics 18 Proceedings of the 18th International Conference on Solid State Ionics Warsaw, Poland, July 3 -8, 2011. doi:http://dx.doi.org/10.1016/j.ssi.2012.04.008.

[39] H. Reschab, C. Cagran, R. Tanzer, W. Schützenhöfer, A. Graf, and G. Pottlacher. Normal spectral emissivity depending on atomic composition for two nickel-based and two ferrous-based alloys at 684.5 nm. 2008. URL: https://pure.tugraz.at/portal/en/publications/normal-spectral-emissivity-depending-on-atomic-composition-for-two-nickelbased-and-two-ferrousbased-alloys-at-6845-nm(e565957f-f777-414e-87e4-300dd0c4b7d3).html.

List of Figures

List of Tables

Acknowledgements

First of all, I would like to thank my supervisor Prof. Gernot Pottlacher, Institute of Experimental Physics and head of the work group *Thermophysics and Metalphysics* for giving me the opportunity to work on this master's thesis. He is always open for questions and discussions and provides me and my colleagues in the work group with a very productive work environment.

Further words of thanks go to the work group: First to Dr. Kirmanj Aziz and Dr. Alexander Schmon, who introduced me to the field of electromagnetic levitation and who were always very helpful and patient with my questions; then of course to Dipl. Ing. Matthias Leitner and Mag. Olivia Klemmer and last but not least to Robert Krisper, who shared the office with me and made the authoring process of this thesis more pleasant by enriching scientific (and non-scientific) debates.

I would like to express my gratitude also to the whole Institute of Experimental Physics and its head Prof. Wolfgang E. Ernst for the opportunity to join the institute. A special thank goes to the secretariat for numerous cases of assistance in administrative matters, the electronics workshop for the prompt repair of the high frequency generator and technical advice as well as to our fine mechanics workshop for the prompt support in cases of mechanical engineering questions concerning the experimental setup.

Finally I would like to thank my close family, especially my parents, who always supported me in all respects.

Graz, September 2016 Thomas Leitner